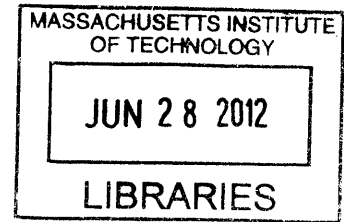


Energy Conversion using Thermal Transpiration: Optimization of a Knudsen  
Compressor

by

Toby A. Klein

B.E. Mechanical Engineering  
Cooper Union, 2010



**ARCHIVES**

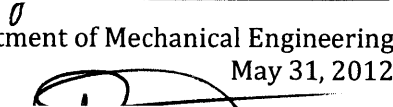
Submitted to the Department of Mechanical Engineering  
in Partial Fulfillment of the Requirements for the Degree of

Master of Science in Mechanical Engineering  
at the  
MASSACHUSETTS INSTITUTE OF TECHNOLOGY

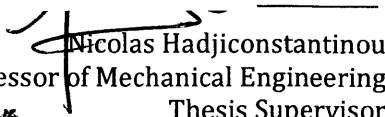
June 2012

©2012 Massachusetts Institute of Technology. All rights reserved.

Signature of Author: \_\_\_\_\_

  
Department of Mechanical Engineering  
May 31, 2012

Certified by: \_\_\_\_\_

  
Nicolas Hadjiconstantinou  
Associate Professor of Mechanical Engineering  
Thesis Supervisor

Accepted by: \_\_\_\_\_

  
David E. Hardt  
Chairman, Departmental Committee on Graduate Students



# Energy Conversion using Thermal Transpiration: Optimization of a Knudsen Compressor

by

Toby A. Klein

Submitted to the Department of Mechanical Engineering  
on May 31, 2012 in Partial Fulfillment of the  
Requirements for the Degree of Master of Science in  
Mechanical Engineering

## ABSTRACT

Knudsen compressors are devices without any moving parts that use the nanoscale phenomenon of thermal transpiration to pump or compress a gas. Thermal transpiration takes place when a gas is in contact with a solid boundary along which a temperature gradient exists. If the characteristic length scale is on the order of, or smaller than, the molecular mean free path, then the gas flows from cold to hot regions.

The nanoscale nature of this phenomenon lends itself to use in nanoscale devices where moving parts are difficult to manufacture. Additional applications include low pressure environments, such as space or vacuum, where molecular mean-free paths are long. Although the flow rates obtained from individual Knudsen compressors are small, reasonable flow rates and significant pressure rises can be attained by cascading a large number of single stages.

In this thesis, we use kinetic-theory based simulations to study thermal transpiration and its application to Knudsen compressors. We simulate such flows in a variety of porous media configurations and then study the effect of various device parameters and operating conditions on the compressor performance.

It is generally observed that generally Knudsen compressors are more efficient when producing a flow than when creating a pressure rise. Small Knudsen numbers and short device lengths tend to increase the mass flow rate, but decrease pressure rise.

Particular attention in our investigation is paid to the compressor efficiency, where a number of efficiency measures are defined, discussed, and compared to previous work in the literature, where available. It is generally found that the Knudsen compressor requires large temperature differences to be competitive as an energy conversion device.

Thesis Supervisor: Nicolas Hadjiconstantinou

Title: Associate Professor of Mechanical Engineering



## ACKNOWLEDGEMENTS

I acknowledge and thank my advisor, Professor Nicolas Hadjiconstantinou, for his insightful advice and guidance in my research and for his constructive, detailed feedback on the drafts of my thesis. I thank the members of Nanoscale Kinetic Transport and Simulation Group for creating a very friendly and supportive lab environment. In particular, I am grateful to Gregg Radtke, who patiently explained his code to me and was always available to answer my questions. Finally, I thank my family and friends for their unwavering support.

# TABLE OF CONTENTS

1	Introduction .....	9
1.1	Motivation.....	9
1.2	Thermal Transpiration.....	9
1.3	Thesis Outline .....	10
2	Theory .....	12
2.1	Converting thermal energy to useful work using a Knudsen Compressor .....	12
2.2	Boltzmann Equation .....	14
2.3	Low Variance Deviational Simulation Monte Carlo (LVDSMC) .....	15
3	Model of Pressure and Flow Rate .....	17
3.1	Single Stage Compressor .....	17
3.2	Multistage Compressor .....	18
4	Simulation .....	21
4.1	Methodology.....	21
4.1.1	Dimensionless Parameters.....	21
4.1.2	Inputs and Boundary Conditions.....	22
4.2	Simulation Geometries .....	22
4.2.1	Case 1: Porous Medium .....	23
4.2.2	Case 2: Realistic 2-D Device Geometry .....	24
4.3	Analysis.....	25
4.3.1	Outputs.....	25
4.3.2	Definitions .....	26
4.4	Results and Discussion .....	27
4.4.1	Porous Medium .....	27
4.4.2	Realistic 2-D Device Geometry .....	28
4.4.3	Statistical Error .....	33
4.4.4	Linearity.....	34
4.4.5	Reversing the Flow through the Compressor.....	35
5	Efficiency.....	37
5.1	Theory .....	37
5.2	Results and Discussion .....	40
5.2.1	Variation with Temperature Ratio.....	40

5.2.2	Ambient Temperature: Cold or Average .....	41
5.2.3	Variation of Efficiency with Different Parameters .....	42
6	Solar Energy: Space Utilization .....	46
6.1	Theory .....	46
6.2	Results and Discussion .....	47
7	Conclusion .....	49
8	Appendix A: Selected Data.....	50
8.1	Additional Statistical Data: .....	50
8.2	Optimal Data for $T_{amb} = T_{cold}$ .....	52
9	Bibliography.....	53

## LIST OF FIGURES

Figure 1-1: Diagram of Knudsen Compressor [1] .....	9
Figure 1-2: Schematic of Thermal Transpiration .....	10
Figure 2-1: Schematic of Knudsen Compressor [1] .....	13
Figure 2-2: Knudsen Compressor [1] .....	14
Figure 3-1: Variation of Pressure Ratio with Knudsen Number ( $Kn_{Lr}$ ) in One Stage .....	18
Figure 3-2: Pressure rise as a function of the Number of Stages .....	19
Figure 3-3: Normalized Conduction Losses as a function of Upflow and Number of Stages .....	19
Figure 4-1: Mesh Grid. Only the Green Area is Simulated. ....	22
Figure 4-2: Porous Medium. Red Arrow Indicates Airflow Direction. Beams are Black. Air is Blue. .	23
Figure 4-3: Porous Medium: Cell Structure Lateral Flow through Beams of Square Cross Section	23
Figure 4-4: 2-D Knudsen Compressor Geometry .....	24
Figure 4-5: Wall Temperature Profile in One Stage of 2-D Knudsen Compressor .....	25
Figure 4-6: Heat Flux through Boundary Cells .....	27
Figure 4-7: Sample Velocity Profile, $Kn = 1.0$ .....	28
Figure 4-8: $m_p/m_T$ in Different Geometries.....	28
Figure 5-1: Aperture Model.....	37
Figure 5-2: Theoretical Efficiency VS Temperature Ratio, with a Pressure Ratio of 1 .....	38
Figure 5-3: Knudsen Compressor: Simulation Model. Linear Temperature Gradient along Boundary.....	38
Figure 5-4: a. Theoretical Heat Input      b. Simulated Heat Input .....	39
Figure 5-5: Variation of Isothermal Efficiency with Temperature Ratio .....	41
Figure 6-1: Schematic for Calculation of Solar Flux Efficiency.....	46

## LIST OF TABLES

Table 4-1: Schematic of Results for Case of $L_x/D_{cap} = 1$ , $Kn_D = 0.5$ , and $L_x = L_y$ .....	29
Table 4-2: Variation of Mass Flow Rate [kg/s/m] with $Kn_D$ , $L_x/D_{cap}$ and $D_{con}/D_{cap}$ .....	31
Table 4-3: Variation of Pressure Ratio with $Kn_D$ , $L_x/D_{cap}$ and $D_{con}/D_{cap}$ .....	32
Table 4-4: Statistical Error in Some Simulated Cases.....	34
Table 4-5: Results for Different Values of Epsilon .....	35
Table 4-6: Forward and Reverse Flow Properties.....	36
Table 5-1: Maximum Difference between Properties with $T_{amb} = T_{ave}$ and $T_{amb} = T_{cold}$ .....	41
Table 5-2: Comparison of Different Definitions of Efficiency, for cases of $T_{amb} = T_{ave}$ .....	43
Table 5-3: Data for Knudsen devices with optimal characteristics, $T_{amb} = T_{ave}$ .....	44
Table 6-1: Variation of Fraction of Space Occupied with Different Parameters .....	48
Table 8-1: Optimal Characteristics for cases where $T_{amb} = T_{cold}$ .....	52



# 1 INTRODUCTION

## 1.1 MOTIVATION

The development of alternative energy sources is a pressing issue, both because of the environmental impact as well as the fact that fossil and nuclear fuels are finite resources. Solar energy is an attractive alternative energy source, due to its abundance and its potential to be exploited at relatively small cost to the environment; as a result, much research has been devoted to harnessing solar energy and converting it into useful work. Photovoltaic cells have received considerable attention in this context. Unfortunately, they are still not able to compete economically with fossil fuels due to material costs and relatively low conversion efficiencies. These efficiencies further diminish relatively quickly due to material degradation and as dirt and dust cover the surface that is exposed to the sun.

The goal of this project is to explore the possibility of exploiting a nanoscale phenomenon known as thermal transpiration to convert thermal energy, from solar or other sources, into useful work. This phenomenon causes gas in contact with a solid surface to move in response to an applied temperature field. Devices known as Knudsen pumps or compressors, an example of which is shown in Figure 1-1, harness this motion to pump or compress the gas. Thermal transpiration is described below.



**Figure 1-1: Diagram of Knudsen Compressor [1]**

## 1.2 THERMAL TRANSPIRATION

Thermal transpiration arises in the presence of a temperature gradient along a solid wall. It can be qualitatively explained by considering the origin of gas particles colliding with a wall along which a temperature gradient exists, as shown in Figure 1-2 (red is hot and blue is cold). Because a particle from the hot region (red) travels faster, on average, than a particle from the cold region, the net force exerted by the particles on the wall is from the hot region to the cold region. The gas therefore experiences an equal force from the wall in the opposite direction, resulting in a net motion of the gas from the cold region to the hot region [2].

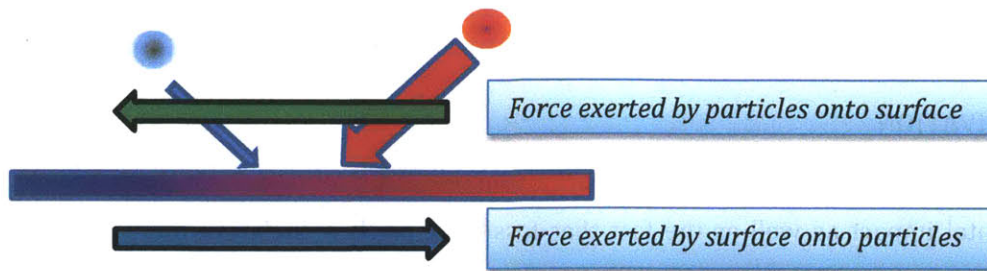


**Figure 1-2: Schematic of Thermal Transpiration**

Thermal transpiration was first explained by Reynolds [3] and Maxwell [4]. The first multistage Knudsen pump was proposed by Knudsen in 1910 [5] and was constructed using an array of heated capillaries. Although not expected to be very efficient, their nanoscale, non-continuum operating principle makes Knudsen compressors unique, and results in specialized features that may be desirable in certain cases. For example, they can be very small, or operate at very low pressures (where molecular mean free path is long, such as space applications [6]). They require no moving parts, lubricants, or sealants, which is a significant advantage, especially for microscale devices [7]. Additionally, because different molecules move at different speeds under the action of thermal transpiration, Knudsen compressors can also be used as gas separators [8].

### 1.3 THESIS OUTLINE

This thesis focuses on the effect of various parameters on the performance of a Knudsen compressor. These parameters include geometry, density, and temperature. The efficiency of the compressor, its capacity to produce flow, and its ability to increase the pressure of a gas stream are evaluated, in the context of maximum energy conversion.

Chapter 2 discusses the theoretical basis for the Knudsen compressor and the simulations used to model it. In Section 2.1, we present methods for theoretically describing thermal transpiration and devices which exploit it, namely Knudsen compressors. In Section 2.2, we present the Boltzmann Equation, which characterizes kinetic transport in gases even where classical fluid mechanics fails. An overview of the method used to simulate the gas flow is reported in Section 2.3.

Chapter 3 presents a mathematical lumped-parameter model of the Knudsen compressor. Single stage compressors are discussed in Section 3.1 and multistage compressors in Section 3.2. This model is capable of predicting the pressure rise and flow rate that a compressor can achieve as a function of geometry and operating parameters.

Chapter 4 discusses our simulation approach in more detail. In Section 4.2.1 we focus on the simulation of thermal transpiration through porous media, while in Section 4.2.2 we study thermal transpiration in realistic 2-D device geometries. In Chapter 5, we present and discuss various measures of Knudsen compressor efficiency, and use simulations to evaluate the efficiency of various geometrical configurations. In Chapter 6, we present calculations for the amount by which solar energy needs to be concentrated to power a Knudsen compressor of the type studied in this thesis. Our conclusions are given in Chapter 7.

## 2 THEORY

In this section, we explain how the phenomenon of thermal transpiration is used in Knudsen compressors. This requires a discussion of the Boltzmann equation, which is used to model a gas at the kinetic level required for capturing this phenomenon. We then give an overview of the theory behind the low-variance deviational simulation used here to model thermal transpiration and devices that exploit it.

### 2.1 CONVERTING THERMAL ENERGY TO USEFUL WORK USING A KNUDSEN COMPRESSOR

Thermal transpiration is the motive force that causes gas molecules in the presence of a solid surface to move from a cold region to a hot one. This phenomenon is negligible in the Navier-Stokes limit of  $Kn \ll 1$ , where  $Kn = \lambda/L$  is the ratio of the molecular mean free path ( $\lambda$ ) to the characteristic flow length scale ( $L$ ). Thermal transpiration is significant for  $Kn \gtrsim 0.1$ , which typically occurs when the density of the gas is low, or when the length scale of the device is small.

Devices which use this phenomenon have been proposed and built by a number of groups [1] [9] [10] [11]. However, using solar energy for providing the temperature gradient (that drives the flow) has only recently been proposed [12] and no such devices have been built. An investigation of the potential of these devices for energy conversion is therefore warranted. We start with a review of the basic principle of operation of a Knudsen compressor.

A typical Knudsen compressor incorporates a number of stages, as a means of achieving large pressure increases. Each stage consists of a capillary and a connector section, as shown in Figure 2-1. The capillary section contains a large number of passages whose transverse dimension is small compared to the molecular mean free path. These passages may be micromachined or could be the pores of a porous membrane. For this reason, the capillary section is sometimes referred to as the compressor membrane.

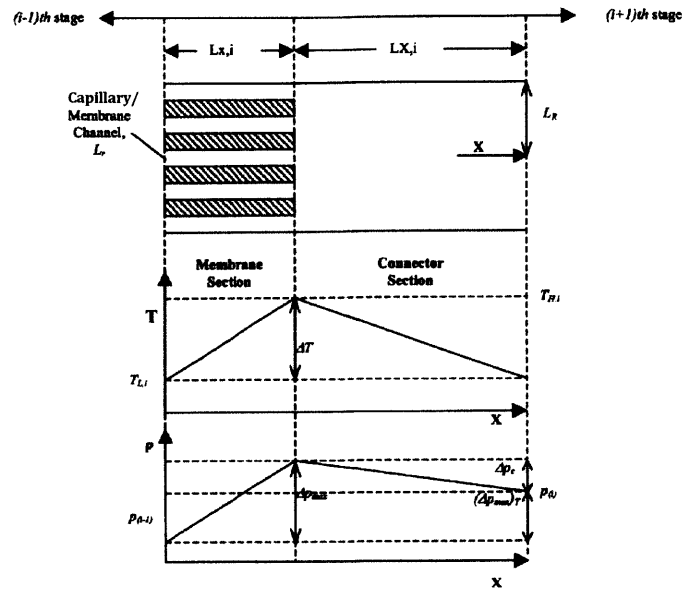


Figure 2-1: Schematic of Knudsen Compressor [1]

The temperature gradient along the capillary section leads to a flow due to thermal transpiration. The temperature gradient is reversed in the connector section, which, due to its "large" transverse scale (much larger than the molecular mean free path), does not cause appreciable reverse thermal transpiration; thus, the reverse flow does not completely cancel the flow created by the capillary section. As a result, in general, a net flow is observed. If the flow is constricted, this will result in a pressure rise, which is largest when the forward flow due to thermal transpiration is equal to the reverse flow due to the pressure gradient in the device. In other words, the maximum pressure increase is obtained when the flow is completely blocked; in the presence of flow, the pressure increase achieved will, in general, be smaller. Conversely, the maximum flow rate is obtained in the limit of no pressure increase.

A diagram of an actual device built at the University of Southern California [1] is shown in Figure 1-1. Figure 2-2 shows the path of the airflow through this device. The "optical radiation" referred to in Figure 2-2 can be supplied by the sun, which is used to heat the aerogel membrane containing the narrow channels of the capillary section. This is followed by the cooler, wide region, which serves the role of the connector.

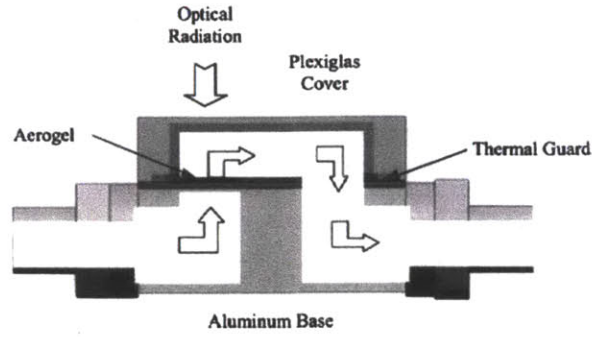


Figure 2-2: Knudsen Compressor [1]

## 2.2 BOLTZMANN EQUATION

Gaseous flows at non-negligible Knudsen numbers (i.e.  $Kn \gtrsim 0.1$ ) can be modeled using the Boltzmann equation [13]:

$$\frac{\partial f}{\partial t} + c_j \frac{\partial f}{\partial x_j} + \frac{F_j}{m} \frac{\partial f}{\partial c_j} = \left[ \frac{\partial f}{\partial t} \right]_{coll} \quad 2.2-1$$

which is a mathematical statement of the conservation of particles in phase space  $(\vec{x}, \vec{c})$ , in terms of the single-particle distribution function  $f(\vec{x}, \vec{c}, t)$ . This is defined such that  $f(\vec{x}, \vec{c}, t)d\vec{x}d\vec{c}$  is the expected number of molecules in the phase space volume between  $(\vec{x}, \vec{c})$  and  $(\vec{x} + d\vec{x}, \vec{c} + d\vec{c})$ . This equation reflects the basic balance between collisionless advection (left hand side of equation 2.2-1), and collisions (right hand side). This balance determines the behavior of the gas, ranging from diffusive (collision dominated) for  $Kn \ll 1$  to ballistic (collisionless) for  $Kn \gg 1$ . The molecular mean free path,  $\lambda$ , which is a measure of the collision rate in the gas, can be determined from the details of the collision term on the right hand side of equation 2.2-1. For a hard-sphere gas, originally studied by Boltzmann [13], the collision operator is given by:

$$\left[ \frac{\partial f}{\partial t} \right]_{coll} = \int_{-\infty}^{\infty} \int_0^{4\pi} (f' f^{*'} - f f^*) c_r \sigma(\Omega) d\Omega d\vec{c}^* \quad 2.2-2$$

where  $\sigma(\Omega)d\Omega$  is the differential collision cross section,  $c_r = |\vec{c} - \vec{c}^*|$  is the relative velocity between a molecule of velocity  $\vec{c}$  and a molecule of velocity  $\vec{c}^*$  with which the former collides,  $f^* = f(\vec{c}^*)$ ,  $f' = f(\vec{c}')$ , and  $f^{*'} = f(\vec{c}^{*'})$ . Here,  $(\vec{c}', \vec{c}^{*'})$  is the post collision velocity pair obtained when the pair of molecules with velocities  $(\vec{c}, \vec{c}^*)$  collide and scatter to solid angle  $\Omega$ . The mean free path for hard-sphere molecules of diameter  $d$  is given by [14]:

$$\lambda = \frac{1}{\sqrt{2} n \pi d^2} \quad 2.2-3$$

where  $n$  is the gas number density defined by [13]:

$$n = \int_{\vec{c} \in R^3} f d\vec{c} \quad 2.2-4$$



Due to the complexity associated with the hard-sphere collision operator 2.2-2, often researchers use the following approximation [15]:

$$\left[\frac{\partial f}{\partial t}\right]_{coll} = \frac{f^{loc} - f}{\tau} \quad 2.2-5$$

referred to as the relaxation time approximation, or Bhatnagar-Gross-Krook (BGK) model [15]. This model replaces the precise dynamics of hard-sphere scattering with the physically based interpretation that collisions tend to drive the distribution function toward the local equilibrium,  $f^{loc}$ . This is an equilibrium (Maxwell-Boltzmann) distribution parametrized by the values of the local gas number density, flow velocity, and temperature [13]; the first is given by equation 2.2-4, while the remaining two are given by:

$$\vec{u} = \frac{\int_{\vec{c} \in R^3} f \vec{c} d\vec{c}}{\int_{\vec{c} \in R^3} f d\vec{c}} \quad 2.2-6$$

$$\frac{3}{2} k_b T = \frac{\int_{\vec{c} \in R^3} \frac{1}{2} m |\vec{c} - \vec{u}|^2 f d\vec{c}}{\int_{\vec{c} \in R^3} f d\vec{c}} \quad 2.2-7$$

respectively, where  $k_b = 1.38 \times 10^{-21}$  J/K is Boltzmann's constant, and  $m$  is the molecular mass.

### 2.3 LOW VARIANCE DEVIATIONAL SIMULATION MONTE CARLO (LVDSMC)

The most prevalent method for solving the Boltzmann equation is the Direct Simulation Monte Carlo (DSMC), a stochastic particle simulation method invented by G.A. Bird [16]. Integration of the Boltzmann equation in time proceeds using a splitting method, i.e. advecting particles in a collisionless fashion (left hand side of 2.2-1) for a time step  $\Delta t$  and then performing collisions for the same time interval (right hand side of 2.2-1), within computational cells of characteristic size  $\Delta x$  [14]. Macroscopic properties are typically sampled in the same computational cells by utilizing their definition in terms of the distribution function (e.g. equations 2.2-6 and 2.2-7) and the fact that in a particle simulation, the distribution function is approximated by:

$$f(\vec{r}, \vec{c}, t) = N_{eff} \sum_i^N \delta(\vec{r} - \vec{r}_i) \delta(\vec{c} - \vec{c}_i) \quad 2.3-1$$

Here,  $N_{eff}$  is the effective number of actual molecules represented by each computational particle, and  $\vec{r}_i(t)$  and  $\vec{c}_i(t)$  are the position and velocity of particle  $i$  at time  $t$ , respectively. The Dirac delta function ( $\delta$ ) samples points to form the discrete representation of the distribution function.

The statistical procedure results in a statistical uncertainty in all macroscopic properties; because the uncertainty decays with the square root of the number of samples taken, this can be a significant limitation in low-speed phenomena [15]. For this reason, in this work we used a recently developed method which alleviates this limitation by simulating only the deviation from

equilibrium. This method is known as Low-Variance Deviational Simulation Monte Carlo (LVDSMC), because it uses deviational particles which simulate the deviation from equilibrium to achieve low variance (statistical uncertainty) solutions of the Boltzmann equation. Despite this fundamental difference, LVDSMC resembles DSMC in its particle nature and the use of a splitting method for integrating in time. LVDSMC was first developed by Homolle and Hadjiconstantinou [17] after the original proposal by Baker and Hadjiconstantinou [18]; it was further refined by Radtke [15]. Radtke and his collaborators also developed efficient deviational methods for simulating the BGK model [19] [20]. The present work utilizes the simulation code described in [15] and [21], which solves the original Boltzmann equation for hard spheres.



### 3 MODEL OF PRESSURE AND FLOW RATE

In this chapter, we describe a theoretical model developed by Muntz et. al. [22] for describing the performance of a single stage and multistage compressor.

#### 3.1 SINGLE STAGE COMPRESSOR

In this lumped-parameter approach [22], each stage is modeled in terms of two coefficients,  $Q_T$  and  $Q_P$ , which, respectively, quantify the thermal transpiration (forward) flow and the reverse flow due to the pressure increase along the device. The coefficients  $Q_T$  and  $Q_P$  contain information about the shape of the duct through which the gas flows and are functions of the Knudsen number; their values for cylindrical channels are reported in Muntz [22]. Values for three dimensional channels of rectangular cross section can be found in [23]. With  $Q_T$  and  $Q_P$  known, the mass flow rate in the Knudsen pump/compressor of cylindrical cross section can be approximated by [22]:

$$\dot{M} = P_{avg} F A \left[ 2 \left( \frac{k_b}{m} \right) T_{avg} \right]^{-1/2} \times \left[ \frac{L_r}{L_z} \frac{\Delta T}{T_{avg}} Q_T - \frac{L_r}{L_z} \frac{\Delta P}{P_{avg}} Q_P \right] \quad 3.1-1$$

where  $L_r$  is the radius of the duct through which the gas flows in the compressor,  $L_z$  the length of the duct, and  $F$  is the fraction of unobstructed duct area,  $A$ .

The pressure rise across the  $i^{\text{th}}$  stage of the compressor,  $P_i$ , can be calculated from [22]:

$$P_i = 1 + \kappa_i \frac{|\Delta T_i|}{T_{avg}} \times \left[ \frac{Q_{T,i}}{Q_{P,i}} - \frac{Q_{T,C,i}}{Q_{P,C,i}} \right] \left[ 1 + \frac{\kappa_i}{2} \frac{|\Delta T_i|}{T_{avg}} \frac{Q_{T,i}}{Q_{P,i}} \right] \quad 3.1-2$$

where the fractional upflow,  $\kappa_i$ , is 1 for zero flow and  $\kappa_i = 0$  for maximum flow. Subscripts containing "C" indicate that this is the value for the connector section. Subscripts without the "C" represent the membrane, or capillary, section. If a property is assumed constant in every stage, the subscript "i" is replaced by the subscript "b".  $\Delta T$  is defined in Figure 2-1.

We illustrate the utility of equation 3.1-2 by calculating the pressure rise as a function of Knudsen number through a cylindrical compressor of the geometry shown in Figure 2-1. The device has a connector to capillary radius ratio of 100, a  $\Delta T$  of 100 K, an average temperature of 293 K and an upflow coefficient,  $\kappa$ , of 0.5. As shown in Figure 3-1, the variation of pressure ratio with compressor Knudsen number in one stage exhibits a maximum at around  $Kn_{Lr} = 15$ , where  $Kn_{Lr}$  is the Knudsen number based on the radius of one of the capillaries.

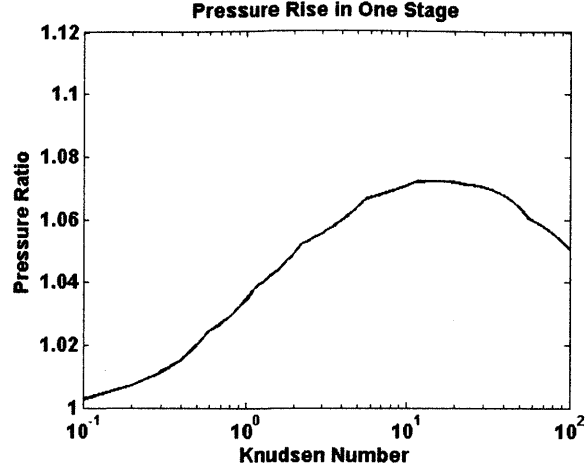


Figure 3-1: Variation of Pressure Ratio with Knudsen Number ( $Kn_{Lr}$ ) in One Stage

### 3.2 MULTISTAGE COMPRESSOR

As stated above, large pressure ratios can be obtained by cascading a large number of stages. The lumped-parameter analysis of Section 3.1 is particularly useful because the desired pressure rise across the whole device,  $(\phi_N)_{DES}$ , can be found by multiplying the pressure ratios of each stage [22]:

$$(\phi_N)_{DES} = \prod_{i=1}^N P_i \quad 3.2-1$$

Figure 3-2 shows the increase in pressure ratio with increasing number of stages, for a Knudsen compressor with an initial  $Kn_{Lr}$  of 1.0 at the entrance. We can see that the performance of Knudsen compressors depends strongly on their geometric characteristics, especially when many single stages are compounded. Specifically, the figure shows that the pressure ratio increases significantly faster if the device radius is adjusted such that the Knudsen number remains constant for each stage. Recall that as the pressure increases along the device, the number density of the gas increases, and thus by equation 2.2-3, the mean free path changes. The Knudsen number of the  $i^{\text{th}}$  stage is given by [22]:

$$Kn_i = Kn_1 \frac{L_{r,1}/L_{r,i}}{\{[P_{AVG,i}/(p_{i-1})_{EFF}] \prod_{s=1}^{i-1} P_s\}} \quad 3.2-2$$

where  $\phi_{i-1} = \prod_{s=1}^{i-1} P_s$  and  $\frac{P_{AVG,i}}{(p_{i-1})_{EFF}} = \left[ 1 + (\kappa_i/2) \frac{|\Delta T_i| Q_{T,i}}{T_{avg} Q_{p,i}} \right]$ . In the case where the radius is constant,  $L_{r,1}/L_{r,i}=1$ , and the resulting pressure rise is significantly smaller than that resulting from a constant Knudsen number of 1.0.

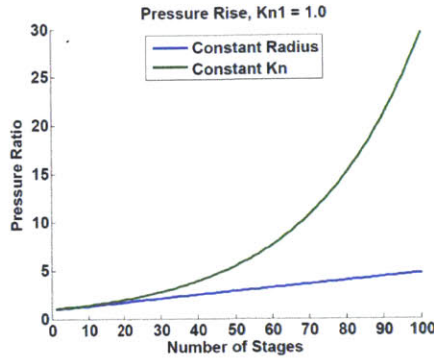


**Figure 3-2: Pressure rise as a function of the Number of Stages**

The model developed by Muntz [22] assumes that all heat losses occur due to conduction through the compressor structure. The heat transfer through the capillary walls of thermal conductivity  $K$  for an  $N$ -stage device is given by:

$$\dot{Q}_N = \sum_{i=1}^N \frac{|T_i|}{L_{z,i}} K_i (1 - F_i) A_i \quad 3.2-3$$

More details about this heat loss and its variation with number of stages and Knudsen number can be found in [22]. As an example, Figure 3-3 shows results for the geometry of Figure 2-1; for these results, we have assumed that the average pressure, temperature, and the fractional upflow remain constant in each stage of the compressor. The optimal  $\kappa_b$  for reducing the heat loss is at around 0.5, and the optimal number of stages is about 45. The results shown are for the cases where

$$(\phi_N)_{DES} = 10 \text{ and } \frac{|\Delta T|}{T_{average}} \frac{Q_T}{Q_P} = 0.1.$$

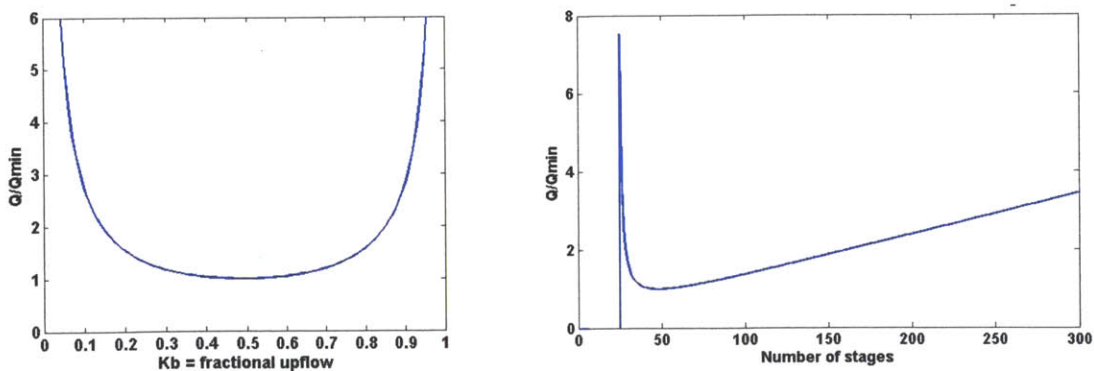


**Figure 3-3: Normalized Conduction Losses as a function of Upflow and Number of Stages**

This mathematical model is useful as a design tool, i.e. for giving approximate values for the mass flow rate and pressure rise of the gas in the Knudsen compressor. Its particular value comes

from its ability to use knowledge of single stage behavior to predict the behavior of multistage devices, which are too large to be simulated at the kinetic level. However, a number of simplifying assumptions are made in this approach. Flow coefficients are derived from a linearized Boltzmann equation; small temperature and pressure gradients are assumed and therefore negligible density changes within the capillary. Channels are assumed to be infinitely long, which is reasonable for capillaries with large lengths compared to their radii, but poor for short connectors with large radii. The only energy use of the compressor is assumed to be from conduction losses through the capillary material. Additionally, recirculation in the transition from capillary to connector section is not accounted for [1]. Moreover, the model does not provide an estimate for the heat input required to run the compressor, nor the entropy generated within it. To determine these quantities, we simulate one stage of the compressor, as described in the next chapter.

## 4 SIMULATION

This chapter presents the simulation methodology and data analysis procedures used for simulating thermal transpiration through porous media and specific Knudsen compressor geometries at the kinetic (Boltzmann) level. Some results are also presented and discussed. Results pertaining to device efficiencies are discussed in Chapter 5.

### 4.1 METHODOLOGY

#### 4.1.1 DIMENSIONLESS PARAMETERS

Simulation results are most frequently presented in terms of non-dimensional quantities. In LVDSMC simulations, non-dimensionalization is achieved using the reference equilibrium from which the deviation is simulated, and a measure of the deviation from equilibrium denoted  $\epsilon$ . Using the subscript "0" to denote equilibrium values, the following non-dimensional quantities (denoted by a hat) are defined:

$$\begin{aligned}
 \text{Time:} \quad \widehat{\Delta t} &= \frac{c_0 \Delta t}{\Delta x} \\
 \text{Length:} \quad \widehat{L}_x &= \frac{L_x}{\text{length scale}} = \frac{L_x}{\left( \frac{\bar{R} T_0}{K n \sqrt{2 \pi} N_a P_0 d^2} \right)} \\
 \text{Temperature:} \quad \widehat{T} &= \epsilon^{-1} \left( \frac{T}{T_0} - 1 \right) \\
 \text{Density:} \quad \widehat{\rho} &= \epsilon^{-1} \left( \frac{\rho}{\rho_0} - 1 \right) \\
 \text{Pressure:} \quad \widehat{P} &= \epsilon^{-1} \left( \frac{P}{P_0} - 1 \right) \\
 \text{Shear:} \quad \widehat{P}_{xy} &= \epsilon^{-1} \left( \frac{P_{xy}}{P_0} \right) \\
 \text{Velocity:} \quad \widehat{u} &= \epsilon^{-1} \left( \frac{u}{c_0} \right) \\
 \text{Heat Flux:} \quad \widehat{q} &= \epsilon^{-1} \left( \frac{q}{c_0 P_0} \right)
 \end{aligned}$$

where  $c_0 = \sqrt{2 \bar{R} T_0}$  is the most probable speed of a gas molecule,  $R = \frac{\bar{R}}{M}$ ,  $\bar{R} = k_b N_a$ , and  $N_a$  is Avogadro's number.  $M$  is the molar mass; the values of  $N_a$  and  $\bar{R}$  are given in 4.3.2.1.

Simulations in this thesis were primarily performed at air densities on the order of  $1 \text{ kg/m}^3$ , which corresponds to a reference pressure slightly below atmospheric. If the compressor is being used in low pressure and density environments, like space, results would have to be scaled accordingly. For example, the length scale of the device increases linearly with a decrease in pressure.

#### 4.1.2 INPUTS AND BOUNDARY CONDITIONS

Simulations were performed using a dimensionless time step  $\widehat{\Delta t} = 1$ , were initialized from equilibrium (zero particles), and were allowed to relax to their steady state before being sampled. We have empirically found that the number of time steps required for steady state to be reached,  $N_{ss}$ , can be estimated by  $N_{ss} \geq N_s = 50 \frac{N_x}{\Delta t}$  (here  $\widehat{\Delta t} = 1$ ), where  $N_x$  is the number of cells in the longest device dimension. In practice, we have taken at least  $2N_s$  time steps before sampling the steady state.

In our simulations, we have modeled solid walls as diffusively reflecting boundaries, since this is typically a reasonable approximation for engineering devices [24]. We have also made extensive use of specular boundary conditions to impose symmetry relations and thus minimize the number of particles required for the simulation. For example, when simulating flow through the square cross-sectional area shown in Figure 4-1, symmetry about the x and y axes allow us to simulate the bottom left corner of the domain, shown in the figure in green, by using specular boundary conditions on the portions on the x and y axes indicated in red.

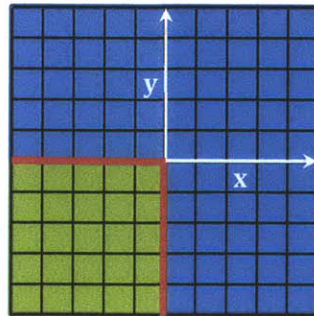


**Figure 4-1: Mesh Grid. Only the Green Area is Simulated.**

## 4.2 SIMULATION GEOMETRIES

Our LVDSMC simulations focused on two distinct geometries and flow scenarios. The objective of the first scenario was to find the effect of the geometry on the ratio between forward thermal transpiration driven flow and reverse pressure driven flow. The performance of the device is maximized by selecting a porous material with maximum forward flow per unit of open area. The second geometry was that of a realistic Knudsen pump, in which the effect of geometrical parameters was investigated.

4.2.1 CASE 1: POROUS MEDIUM

Flow through a regular porous medium was modeled by simulating a square periodic domain with variable hydraulic diameter ( $D_h$ ) as a result of rectangular constrictions (shown in black in Figure 4-2). This study is of interest because recent Knudsen compressor designs use porous materials (e.g. aerogel [25]) for their capillary section.

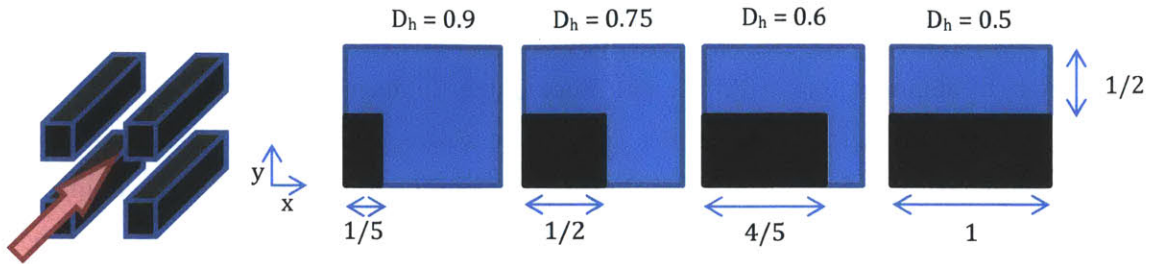


Figure 4-2: Porous Medium. Red Arrow Indicates Airflow Direction. Beams are Black. Air is Blue.

The geometry shown on the left in Figure 4-3, which interpolates between the porous medium of Figure 4-2 and the rectangular channels that are typical in microscale devices, was also investigated. Figure 4-3 shows the case with  $D_h=0.75$ . Our results are compared to results from simulations by Doi [23], who computed the flow coefficients for rectangular channels of varying aspect ratios (AR). It is also compared with flow through cylindrical tubes, as reported by Muntz [22] and with lateral flow across beams of square cross section (shown on the right in Figure 4-3).

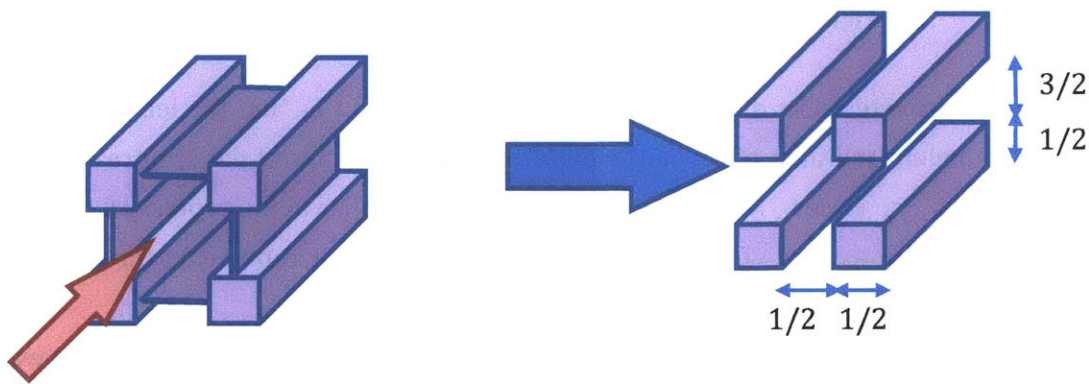


Figure 4-3: Porous Medium: Cell Structure      Lateral Flow through Beams of Square Cross Section

A typical simulation ran for 500,000 time steps; the first 10,000 time steps were used to reach steady state. There were 100 cells in both the x and y directions, and about 10 molecules per cell. Simulations with more transient steps and more time steps were also run to check the accuracy



of the results. Independent runs were made for thermal transpiration driven flow and pressure driven flow. In order to reduce computational cost, all simulations were run as 2 dimensional (in the cross-sectional plane); flow normal to this plane, whether pressure or thermal-transpiration driven, was created by the body force approach explained by Radtke [15]. Our results are presented in Section 4.4.1.

#### 4.2.2 CASE 2: REALISTIC 2-D DEVICE GEOMETRY

In order to obtain estimates for the efficiency of the Knudsen compressor, and to further optimize it, a large number of simulations of realistic single-stage devices were performed, exploring the large parameter space available. In order to limit the computational cost, simulations were performed in two dimensions on the geometry shown in Figure 4-4. In this figure, the single-stage simulated is shown in dark color. The two-dimensional assumption amounts to simulating a device that is very long in the third dimension (into the paper).

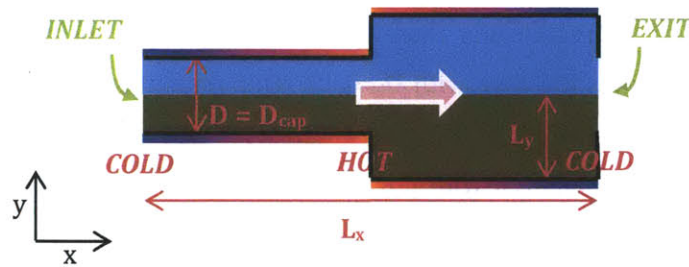


**Figure 4-4: 2-D Knudsen Compressor Geometry**

Geometric parameters like the lateral dimension  $D$ , the height  $L_y$ , and the length  $L_x$  were varied in order to understand their effect on the performance of one stage of the compressor. The Knudsen number was also varied.  $Kn_D$  represents the Knudsen number in the capillary section of height  $D$ , also referred to as  $D_{cap}$ . The symbol  $Kn$  without a subscript represents the Knudsen number based on the length scale  $L_y$ , which is half of the connector height,  $D_{con}$ .

The linear temperature profile imposed on the device walls is shown in Figure 4-5. The wall temperature increases linearly from  $T_{cold}$  to  $T_{hot}$ , then decreases linearly back to  $T_{cold}$ . The average temperature,  $T_{ave}$  is assumed to be the equilibrium temperature,  $T_0$ , and the ambient temperature,  $T_{amb}$ . We performed simulations with varying temperature gradients and with  $T_0 = T_{cold}$ . Selected results are presented in Sections 4.4 and 5.2.



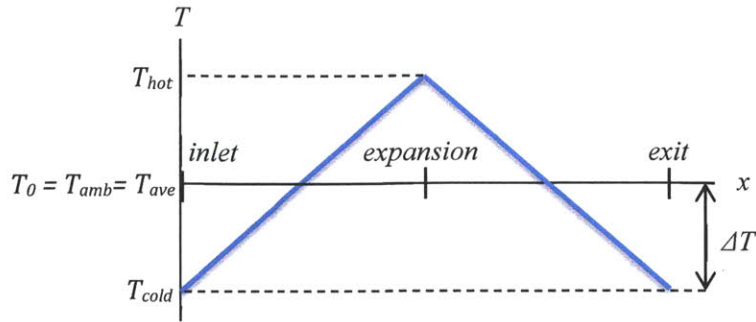


**Figure 4-5: Wall Temperature Profile in One Stage of 2-D Knudsen Compressor**

The deviation from equilibrium,  $\epsilon$ , is defined using the temperature gradient:  $\epsilon = \frac{\Delta T}{T_0}$ . Often, our conditions of interest are  $\Delta T = 100$  K and  $T_0 = 298$  K; in other words, the temperature varies linearly between  $T_{\text{cold}}=198$  K to  $T_{\text{hot}}=398$  K. This corresponds to an  $\epsilon$  of 0.34. Most simulations were performed with  $\epsilon = 0.0001$ , and the results scaled such that they corresponded to  $\epsilon = 0.34$ . The validity of this linearity assumption is investigated in Section 4.4.4.

A typical simulation ran for 1,002,000 time steps, with the first 5,000 or 10,000 steps used to reach steady state. There were between 20 and 100 cells in the  $x$  and  $y$  directions, 40 being most typical, and about 10 molecules per cell. Simulations with more transient steps, more time steps, and more molecules per cell were also run to check the accuracy of the results.

Two types of simulations were run to calculate the maximum mass flow rate and maximum pressure rise. For both cases, the boundary conditions at the walls are diffuse. To find the maximum mass flow rate in an infinite number of stages, the boundary conditions at the inlet and exit were set to be periodic. To find the maximum pressure rise, the flow rate must be zero; this is achieved by using specular boundary conditions at the inlet and exit of the compressor.

### 4.3 ANALYSIS

In this section, we discuss the methodology for analyzing the simulation results reported in Section 4.4.

#### 4.3.1 OUTPUTS

The simulation code outputs cell-averaged values of dimensionless properties and cell-surface-averaged properties on the outer surfaces of the boundary cells. The output cell properties are density, velocity, pressure, stress, temperature, and heat flux. The boundary properties are

pressure and heat flux. Multiple runs of the same simulation were made to determine the statistical error (see Section 4.4.3 and Chapter 8: Appendix A for data on the statistical error).

### 4.3.2 DEFINITIONS

#### 4.3.2.1 Length scale

The mean free path of the gas was determined from the number density,  $n$ , and the molecular size,  $\sigma = 3.5 \text{ \AA}$ , where:

$$n = \frac{\rho}{M} N_a = \frac{P}{\bar{R}T} N_a \quad N_a = 6.02 \times 10^{26} \frac{\text{molecules}}{\text{kmol}} \quad \bar{R} = 8\,314 \frac{\text{J}}{\text{kmol} \cdot \text{K}}$$

The length scale of the device is taken to be the dimensionless length of 1. From the mean free path of the gas, and the Knudsen number that is an input parameter, the dimensional length scale of the device is determined as  $L = \lambda/\text{Kn}$ . To determine the dimensions  $L_x$  and  $L_y$  of the device (defined in Figure 4-4), we must multiply the dimensionless lengths input to the code,  $\hat{L}_x$  and  $\hat{L}_y$ , by the length scale,  $L$ :  $L_x = \hat{L}_x \times L$  and  $L_y = \hat{L}_y \times L$ . If the Knudsen number is changed, but the length scale must remain constant, the reference pressure in the device is changed so that the mean free path adjusts to scale with Kn.

#### 4.3.2.2 Pressure Ratio

The inlet pressure is determined by averaging the values of the pressure for all the cells located at the inlet. The exit pressure is similarly determined. The pressure ratio is the exit pressure divided by the inlet pressure. The inlet and exit are shown in Figure 4-4.

#### 4.3.2.3 Mass flow rate

The mass flow rate per unit depth ( $\dot{m}/\text{depth}$ ) is measured midway along the capillary, where density variations are small, and is therefore approximately given by  $\dot{m}/\text{depth} \approx \rho_0 \sum_i v_i \Delta y_i$ , where the sum runs over all cells at the station of interest. The equilibrium density is denoted  $\rho_0$ , and  $v_i$  and  $\Delta y_i$  are the velocity and height (in the y-direction) of cell  $i$ . The average flow velocity is given by  $u_{cap} = \frac{\dot{m}}{\rho_0 \cdot D \cdot \text{depth}}$  for the capillary section. Refer to Figure 4-4 for the definition of  $D$  and  $L_y$ .

#### 4.3.2.4 Heat Transfer and Entropy

Heat interactions with the environment were calculated by summing individual contributions of appropriate boundary cells. For example,  $Q_{total}$ , the net energy per unit depth transferred through the walls of the device, was calculated using  $Q_{total} = 2 \sum_i q_i \Delta l_i$ , where  $q_i$  denotes the heat flux through boundary cell  $i$  and  $\Delta l_i$  denotes the length of this cell along the boundary. The factor of 2 accounts for the fact that, due to symmetry, only half of the boundary cells are simulated (see Figure 4-4). The index  $i$  runs through all boundary cells through which heat is transferred to the device (i.e. the ones with a specified temperature, on which reflection is

diffuse), as shown in Figure 4-6. Similarly, the entropy exchange with the environment is given by  $S_{total} = 2 \sum_i \frac{q_i}{T_i} \Delta l_i$ , where  $T_i$  denotes the temperature at boundary cell  $i$ . Heat flux is positive when flowing out of the device.

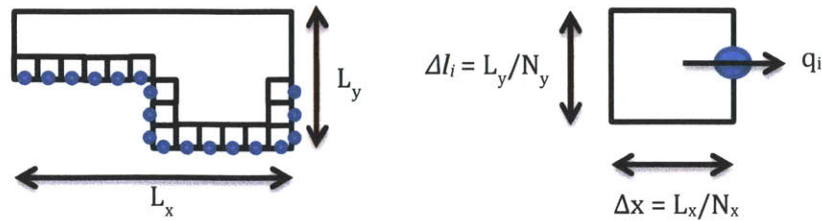


**Figure 4-6: Heat Flux through Boundary Cells**

Note that the simulation assumes ideal materials with no conduction along walls. This is probably not a safe assumption because the device is so small; Muntz [22] approximates conduction losses along the length of the Knudsen pump, as mentioned in Section 3.2. However if the device is used in space applications, where it is a large device working on a low density gas, the ideal assumption may be valid.

## 4.4 RESULTS AND DISCUSSION

### 4.4.1 POROUS MEDIUM

To find the optimal geometry for the capillary section of the Knudsen compressor, the thermal transpiration driven flow must be maximized and the pressure driven flow minimized. This is easily seen from equation 4.4-1 [22], presented in Section 3.1 and again below, which shows that thermal transpiration drives the flow forward, and the pressure gradient opposes the flow.

$$\dot{M} = P_{avg} F A \left[ 2 \left( \frac{k_b}{m} \right) T_{avg} \right]^{-1/2} \times \left[ \frac{L_r}{L_z} \frac{\Delta T}{T_{avg}} Q_T - \frac{L_r}{L_z} \frac{\Delta P}{P_{avg}} Q_P \right] \quad 4.4-1$$

Thermal transpiration driven flows were simulated and the velocity profile (see Figure 4-7) and mean velocity were obtained. The dimensionless mean velocity,  $m_T = \frac{u_z}{c_0 \epsilon}$ , corresponds to  $\frac{1}{4}$  of the constant  $Q_T$  shown in equation 4.4-1. Pressure driven flows were also simulated; the dimensionless mean velocity in these simulations was  $m_P = \frac{1}{4} Q_P$ . The ratio of  $m_P/m_T$  was plotted for the various cases. The results are shown in Figure 4-8.

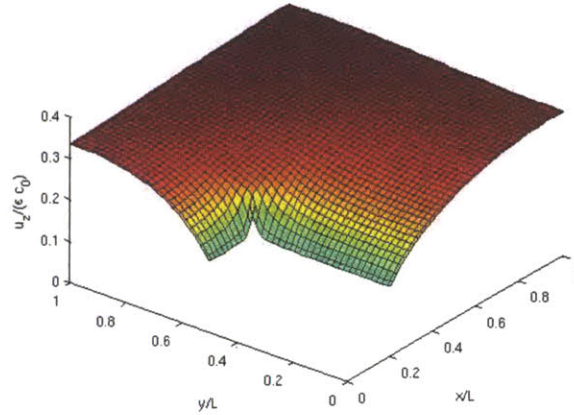


Figure 4-7: Sample Velocity Profile,  $Kn = 1.0$

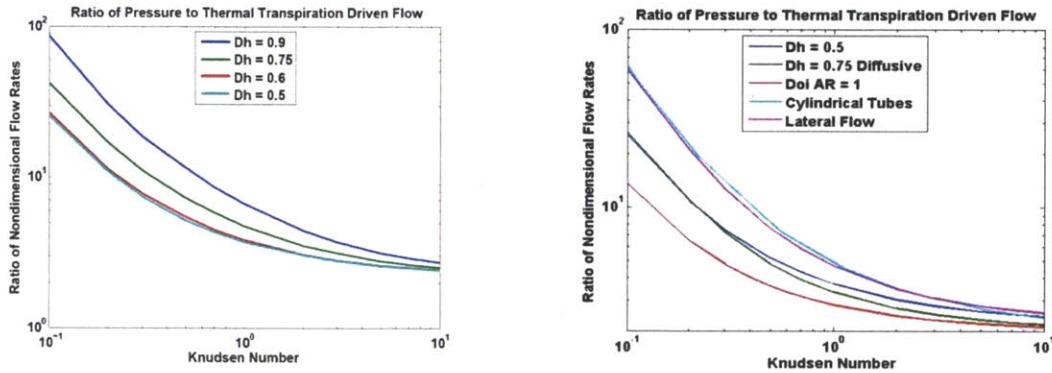


Figure 4-8:  $m_P/m_T$  in Different Geometries

The left plot in Figure 4-8 compares the geometries shown in Figure 4-2. The right plot compares the best case of those in the left plot, a slit (“ $Dh = 0.5$ ”), with the cell structure shown in Figure 4-3 (“ $Dh = 0.75$  Diffusive”), a hollow square channel (“ $Doi\ AR = 1$ ” [23]), a hollow cylindrical tube [22], and flow laterally over beams of square cross section (Figure 4-3). The optimal case (of the configurations simulated) was that of a square channel, because it minimizes  $m_P/m_T$ .

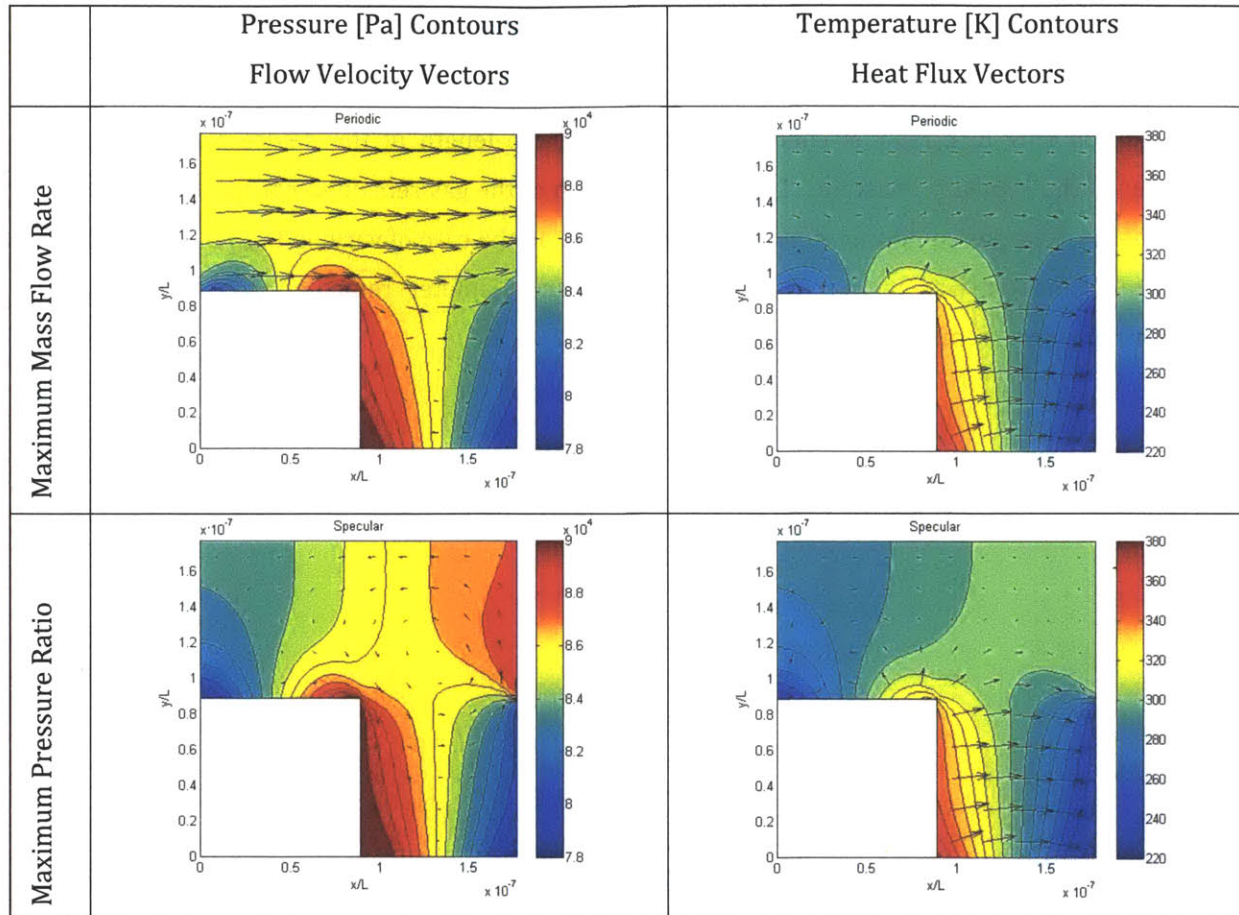
#### 4.4.2 REALISTIC 2-D DEVICE GEOMETRY

The majority of our simulations focused on optimizing the parameters of a more realistic, 2-dimensional model of the Knudsen compressor. Sample plots of the base case with  $L_x/D_{cap} = 1$  and  $Kn_D = 0.5$  are shown in Table 4-1. In this case, the ambient air temperature ( $T_{amb} = T_0$ , the equilibrium temperature) was set to the average air temperature ( $T_{average} = 0.5(T_{hot} + T_{cold}) = 298\text{ K}$ ). Both the maximum flow rate (periodic boundary condition) and the maximum pressure ratio



(specular boundary condition) cases are shown, with contours representing either pressure or temperature, and vectors showing the flow velocity or heat flux through the gas.

**Table 4-1: Schematic of Results for Case of  $L_x/D_{cap} = 1$ ,  $Kn_D = 0.5$ , and  $L_x = L_y$**



We also investigated the effect of ambient temperature by comparing the cases  $T_{amb} = T_{ave}$ , and  $T_{amb} = T_{cold}$ . The variation in mass flow rate is shown in Table 4-2; the variation in pressure ratio is shown in Table 4-3. For the base case, the temperature of the wall ranged linearly from 198 K to 398 K, the density was 1 kg/m<sup>3</sup> and the pressure was 85496 Pa when  $T_{amb} = 298$  K; the base case for where  $T_{amb} = T_{cold}$  was different only in that  $T_{amb}$  became 198 K and the pressure became 56806 Pa. Note that the ambient pressure was changed as necessary to keep the length scale of the device constant despite the change in Knudsen number (rows A and B of Table 4-2 and Table 4-3), as explained in Section 4.3.2.1. This was necessary so that we could compare the effects of the change in Knudsen number on the device, without the additional effects of a change in length.

The density of the gas was adjusted to correspond to the new pressure. Although the entering and exiting pressure changed, the pressure ratio remained the same. However, the mass flow rate changed because of the change in density.

In row C of Table 4-2 and Table 4-3,  $L_x/D_{cap}$  is varied by decreasing the diameter of the capillary and keeping the length of the device constant. In order to keep the Knudsen number in the capillary constant, the mean free path of the gas, and therefore the ambient pressure, was adjusted. In row E,  $L_x/D_{cap}$  is changed by adjusting the length of the device and holding the diameter of the capillary constant. The mean free path of the gas remained constant; the pressure and density of the gas could therefore remain constant. In the case of varying  $D_{con}/D_{cap}$  (row D), the connector diameter was increased while the capillary diameter remained constant.  $Kn_D$ , and therefore pressure, remained constant.

**Table 4-2: Variation of Mass Flow Rate [kg/s/m] with  $Kn_D$ ,  $L_x/D_{cap}$  and  $D_{con}/D_{cap}$**

	$T_{amb} = T_{average}$	$T_{amb} = T_{cold}$
A. Constant $L_x/D_{cap}=1$		
B. Constant $L_x/D_{cap}=4$		
C. Decreasing $D_{cap}$ , $Kn_D=6$ , constant $L_x$		
D. Increasing $D_{con}$ , $Kn_D=6$		
E. Increasing $L_x$ , $Kn_D=0.5$ , const $D_{cap}$		

**Table 4-3: Variation of Pressure Ratio with  $Kn_D$ ,  $L_x/D_{cap}$  and  $D_{con}/D_{cap}$**

	$T_{amb} = T_{average}$	$T_{amb} = T_{cold}$
A. Constant $L_x/D_{cap}=1$		
B. Constant $L_x/D_{cap}=4$		
C. Decreasing $D_{cap}$ , $Kn_D=6$ , constant $L_x$		
D. Increasing $D_{con}$ , $Kn_D=6$		
E. Increasing $L_x$ , $Kn_D=0.5$ , const $D_{cap}$		



It is apparent from the tables that the pressure ratio is unaffected by the lower ambient air temperature. The mass flow rate, however, tends to be slightly higher when the ambient temperature is low, though it is on the same order of magnitude as the cases where the ambient temperature is the average temperature. The overall trends, however, are the same. When  $L_x/D_{cap}$  is constant, increasing the Knudsen number decreases the mass flow rate and increases the pressure ratio up to a  $Kn_D$  of about 3, where both the pressure ratio and mass flow rate become constant (row A). When  $Kn_D$  is constant, increasing  $L_x/D_{cap}$  decreases the mass flow rate and increases the pressure ratio. There appears to be a peak in the pressure ratio at about  $L_x/D_{cap}$  of 3, with a slight decrease in pressure ratio for higher values of  $L_x/D_{cap}$  (row E). The pressure ratio increases with increasing  $D_{con}/D_{cap}$ , while the mass flow rate slightly decreases (row D).

Thermal transpiration is negligible for small Knudsen numbers, and becomes increasingly more prominent through the transition region until the  $Kn$  is so high that the flow is essentially ballistic. This accounts for the increase in pressure ratio and its subsequent asymptotic behavior as the Knudsen number increases. It also accounts for a similar behavior as  $D_{con}/D_{cap}$  increases. The smaller the capillary diameter, the larger the forward flow; the larger the connector diameter, the smaller the reverse flow. However, there comes a point where forward flow is at its maximum and reverse flow is at its minimum and increasing  $D_{con}/D_{cap}$  beyond that does not yield a higher pressure ratio.

#### 4.4.3 STATISTICAL ERROR

In order to determine the statistical error associated with our simulation results, we performed multiple simulations with identical parameters but different random number seeds. We also investigated the effect of varying the number of simulation cells and the number of simulation particles per cell. A subset of the results is reported in Table 4-4; for more complete results, see Section 8.1.

In the first column of Table 4-4, a case with a temperature ratio of 5 and ambient temperature equal to the low temperature is shown. This case was simulated multiple times with  $\epsilon = 0.1$  and once with  $\epsilon = 0.0001$ , and the results were not significantly different (for further discussion of this linearity assumption see Section 4.4.4). The results from the periodic and specular simulations for another case are shown in the last two columns of the table. In all cases, the only properties with a standard deviation on the order of their mean values are the heat flux and net heat exchange,  $Q_{flux}$  and  $Q_{total}$ , respectively. This is because these quantities are close to zero. Comparing  $Q_{total}$  to  $Q_{in}$ , which is the sum of all the heat entering the device, it is evident that  $Q_{total}$  is several orders of magnitude lower. Similarly,  $Q_{flux}$  is orders of magnitude below  $Q_{max}$ , which

is the maximum heat flux through a cell boundary. Note that because the normal vector on the device points outward, negative values for  $Q$  and  $S$  indicate inward flow ( $Q_{in}$  has already accounted for this, so positive values indicate an inward flow). Positive values for  $S$  therefore indicate that entropy is being generated and then rejected from the device, as we would expect.

**Table 4-4: Statistical Error in Some Simulated Cases**

Boundary Condition	Periodic		Periodic		Specular	
	Mean Value	Standard Deviation	Mean Value	Standard Deviation	Mean Value	Standard Deviation
$T_{ratio}$	5		2		2	
$T_{hot}$	1000		398		398	
$T_{cold}$	200		198		198	
$T_{amb}$	200		298		298	
$L_x/D_{cap}$	3		10		10	
$Kn_D$	0.5		0.5		0.5	
$D_{con}/D_{cap}$	2		2		2	
$L_x/L_y$	3		10		10	
$L_x$	5.31E-07		1.77E-06		1.77E-06	
$L_{x0}$	2.65E-07		8.84E-07		8.84E-07	
$L_y$	1.77E-07		1.77E-07		1.77E-07	
$L_{y0}$	8.84E-08		8.84E-08		8.84E-08	
$D_{cap}$	1.77E-07		1.77E-07		1.77E-07	
$N_x$	40	0	40	0	40	0
$N_y$	40	0	60	34.64	60	34.64
$u$ (cap) [m/s]	2.89E+01	1.70E-01	2.15E+00	5.84E-02	-2.95E-01	1.19E-02
massflow [kg/m/s]	5.11E-06	3.01E-08	3.81E-07	1.03E-08	-5.22E-08	2.11E-09
$P_{enter}$ [Pa]	5.74E+04	0.00E+00	8.55E+04	0.00E+00	8.02E+04	3.51E+00
$P_{exit}$ [Pa]	5.74E+04	0.00E+00	8.55E+04	0.00E+00	8.60E+04	5.29E+00
$P_{ratio}$	1.00E+00	0.00E+00	1.00E+00	0.00E+00	1.07E+00	1.15E-04
$Q_{flux}$ [W/m <sup>2</sup> ]	-1.34E+05	2.47E+04	8.15E+02	5.79E+02	4.70E+04	1.85E+03
$S_{flux}$ [W/m <sup>2</sup> /K]	4.20E+04	1.01E+03	3.58E+03	2.19E+01	3.78E+03	2.22E+01
$Q_{max}$ [W/m <sup>2</sup> ]	2.10E+07	5.02E+05	2.79E+06	1.16E+04	2.92E+06	8.09E+03
$S_{max}$ [W/m <sup>2</sup> /K]	1.05E+05	2.51E+03	1.41E+04	5.86E+01	1.47E+04	4.06E+01
$Q_{total}$ [W/m]	-1.04E-01	2.63E-03	-1.78E-03	1.46E-03	-2.50E-04	6.15E-04
$S_{total}$ [W/m/K]	1.99E-02	2.26E-04	3.16E-03	1.21E-05	3.12E-03	5.39E-06
$Q_{in}$ [W/m]	6.89E+00	7.61E-02	1.63E+00	2.32E-03	1.62E+00	2.45E-03
$S_{in}$ [W/m/K]	7.53E-03	8.48E-05	4.36E-03	5.69E-06	4.31E-03	6.21E-06

#### 4.4.4 LINEARITY

As explained in Section 4.2.2, most of our simulations were performed with  $\epsilon=0.0001$  (corresponding to  $\Delta T = \epsilon T_0 = 0.03$  K for  $T_0 = 298$  K); results for different  $\Delta T$  were obtained by assuming a linear response. As many of our simulations had larger deviations, it was important to verify that changing  $\epsilon$ , the departure from equilibrium, would not deleteriously affect the integrity

of the results. We therefore ran simulations with input values of  $\epsilon=0.335$  and  $\epsilon=0.667$ , which correspond, respectively, to  $\Delta T = 100$  K and  $\Delta T = 200$  K for  $T_0= 298$  K. We compared these to our results for  $\epsilon=0.0001$ , which was an arbitrary small value of  $\epsilon$ . Table 4-5 represents these results, scaled such that they correspond to  $\epsilon = 100/298 = 0.335$ , i.e. a  $\Delta T$  of 100 K at  $T_0= 298$  K. In these simulations, we used periodic boundary conditions,  $T_{\text{amb}} = T_{\text{ave}}$ ,  $L_x/D_{\text{cap}} = 3$ ,  $Kn_D = 0.5$ , and  $D_{\text{con}}/D_{\text{cap}} = 2$ . The results in Table 4-5 include standard deviations and percentage deviation from the  $\epsilon=0.0001$  case. The values of  $Q_{\text{flux}}$  and  $Q_{\text{total}}$  are the only ones that fluctuate significantly, and they are assumed to be inconsequential, as shown in the analysis in Section 4.4.3. They are not used in any of the subsequent calculations.

**Table 4-5: Results for Different Values of Epsilon**

<b>eps</b>	<b>0.0001</b>	<b>0.3356</b>	<b>0.6711</b>	<b>Std Dev</b>	<b>% Dev</b>
<b><math>u_{\text{cap}}</math> [m/s]</b>	5.9736	6.0241	6.5445	0.3160	5.2906
<b>massflow</b> [kg/m/s]	1.06E-06	1.07E-06	1.16E-06	5.6E-08	5.2920
<b><math>P_{\text{enter}}</math> [Pa]</b>	85496	85496	85496	0	0
<b><math>P_{\text{exit}}</math> [Pa]</b>	85496	85496	85496	0	0
<b><math>P_{\text{ratio}}</math></b>	1	1	1	0	0
<b><math>Q_{\text{flux}}</math> [W/m<sup>2</sup>]</b>	1244.9	99664	2.88E+05	145915	11721
<b><math>S_{\text{flux}}</math> [W/m<sup>2</sup>/K]</b>	8145.5	8484.5	9113.9	491.40	6.0328
<b><math>Q_{\text{max}}</math> [W/m<sup>2</sup>]</b>	6.08E+06	6.24E+06	6.51E+06	215031	3.5364
<b><math>S_{\text{max}}</math> [W/m<sup>2</sup>/K]</b>	30710	31534	32862	1085.79	3.5356
<b><math>Q_{\text{total}}</math> [W/m]</b>	0.0011	-0.0023	-0.0039	0.0026	233.79
<b><math>S_{\text{total}}</math> [W/m/K]</b>	0.0041	0.0040	0.0040	4.3E-05	1.0512
<b><math>Q_{\text{in}}</math> [W/m]</b>	1.9917	1.9750	1.9189	0.0381	1.9138
<b><math>S_{\text{in}}</math> [W/m/K]</b>	0.0053	0.0052	0.0051	8.3E-05	1.5772

#### 4.4.5 REVERSING THE FLOW THROUGH THE COMPRESSOR

In this section, we investigate whether reversing the driving force in a Knudsen compressor results in a reverse flow with the same magnitude. In other words, when  $\epsilon$  is made negative, we determine whether it is safe to assume that the mass flow rate and pressure ratio that are produced by this reverse flow are equal to those produced by the forward flow. This is simulated by inverting the temperature gradient shown in Figure 4-5. The results for  $T_{\text{ratio}} = 2$  ( $T_{\text{hot}} = 398$  K,  $T_{\text{cold}} = 198$  K,  $T_{\text{amb}} = 298$  K,  $L_x/D_{\text{cap}} = 3$ ,  $Kn_D = 0.5$ ,  $L_x=5.31 \text{ E } -7$  m), are shown in Table 4-6. The pressure ratio for the reverse case is defined as the inverse of the pressure ratio for the forward case, as the inlet and the exit have switched positions.

**Table 4-6: Forward and Reverse Flow Properties**

	Periodic		Specular	
	Forward	Reverse	Forward	Reverse
$u_{cap}$ [m/s]	5.97E+00	-5.96E+00	-1.37E-02	2.88E-02
massflow [kg/m/s]	1.06E-06	-1.05E-06	-2.42E-09	5.10E-09
$P_{enter}$ [Pa]	8.55E+04	8.55E+04	8.31E+04	8.79E+04
$P_{exit}$ [Pa]	8.55E+04	8.55E+04	8.93E+04	8.17E+04
$P_{ratio}$	1.000	1.000	1.075	1.077
$Q_{flux}$ [W/m <sup>2</sup> ]	1.24E+03	9.96E+02	1.16E+05	-1.17E+05
$S_{flux}$ [W/m <sup>2</sup> /K]	8.15E+03	8.15E+03	8.42E+03	7.51E+03
$Q_{max}$ [W/m <sup>2</sup> ]	6.08E+06	6.09E+06	6.25E+06	5.76E+06
$S_{max}$ [W/m <sup>2</sup> /K]	3.07E+04	3.07E+04	3.16E+04	2.91E+04
$Q_{total}$ [W/m]	1.10E-03	8.16E-04	4.47E-04	-8.96E-04
$S_{total}$ [W/m/K]	4.05E-03	4.05E-03	3.94E-03	3.91E-03
$Q_{in}$ [W/m]	1.99E+00	1.99E+00	1.93E+00	1.93E+00
$S_{in}$ [W/m/K]	5.27E-03	5.27E-03	5.12E-03	5.11E-03

It is apparent from Table 4-6 that the forward and reverse mass flow rates (obtained by applying periodic boundary conditions) and pressure ratios (obtained by applying specular boundary conditions) are approximately equal, as are most of the other outputs.  $Q_{in}$  and  $S_{total}$ , which are other parameters used in measuring efficiency (Section 5.1), also remain the same when flow is reversed.



To obtain the efficiency, the work is divided by the heat input. However, they first normalize each term by its corresponding mass flow rate. Thus:

$$\eta = \frac{\dot{W}}{\dot{Q}} = \frac{\left(\frac{\dot{m}_{HOT} P_{HI}}{\rho_{HOT}} / \dot{m}_{HOT} - \frac{\dot{m}_{COLD} P_{LO}}{\rho_{COLD}} / \dot{m}_{COLD}\right)}{(\dot{m}_{HOT} + \dot{m}_{COLD}) c_p \Delta T / \dot{m}_{NET}} = \frac{\frac{P_{HI}}{\rho_{HOT}} - \frac{P_{LO}}{\rho_{COLD}}}{(\dot{m}_{HOT} + \dot{m}_{COLD}) c_p \Delta T / \dot{m}_{COLD} - \dot{m}_{HOT}} \quad 5.1-1$$

From here, they simplify to:

$$\eta = \frac{R}{c_p} \left( \frac{\Gamma_{COLD} - \Gamma_{HOT}}{\Gamma_{COLD} + \Gamma_{HOT}} \right) = \frac{R}{c_p} \left( \frac{\sqrt{T_{HOT}/T_{COLD}} - P_{HOT}/P_{COLD}}{P_{HOT}/P_{COLD} + \sqrt{T_{HOT}/T_{COLD}}} \right) \quad 5.1-2$$

The plot of efficiency with respect to temperature ratio for different gases is shown in Figure 5-2. Note that in this plot, the pressure ratio is assumed to be one. Although the justification for a number of steps in this derivation is unclear, Copic and NcNamara point out that this result seems to approach the correct limits and predicts rapid reduction in the efficiency at pressure ratios greater than one [26], which is supported by our results.

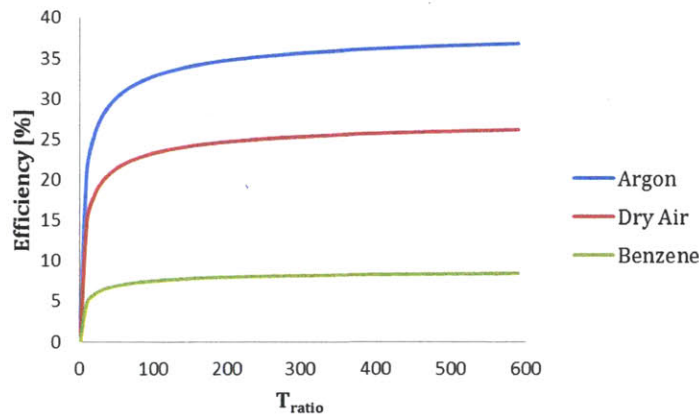


Figure 5-2: Theoretical Efficiency VS Temperature Ratio, with a Pressure Ratio of 1

Alternatively, a measure of the efficiency of the compressor can be derived by imagining a turbine affixed to the exit of a Knudsen compressor, as shown in Figure 5-3. If the ambient temperature is equal to the temperature of the gas at the outlet of the compressor, the ideal gas expands isothermally through the turbine, generating work,  $\dot{W}_{iso} = \dot{m} R T_{amb} \ln \frac{P_{HI}}{P_{LO}}$  ( 5.1-3 ).

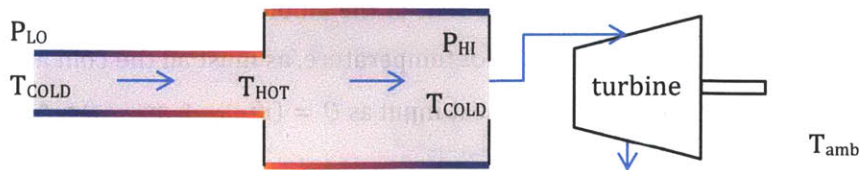


Figure 5-3: Knudsen Compressor: Simulation Model. Linear Temperature Gradient along Boundary.

In Section 5.2.1, we present results assuming that the ambient temperature is equal to the average of the hot and cold temperatures; in this case, the turbine is assumed to be operating at the average temperature. We also present results in which the ambient temperature was set to be equal to the cold temperature; this is more realistic, and is consistent with the assumptions made by Copic and McNamara [26]. Expression 5.1-3 will be used throughout the thesis even when the ambient temperature is equal to the cold outlet temperature. In Section 5.2.2 we compare simulations of  $T_{amb} = T_{cold}$  to  $T_{amb} = T_{ave}$ , and resolve that they are similar enough to proceed with  $T_{amb} = T_{ave}$ .

The isothermal efficiency can be calculated from the simulation as follows. The flow rate is evaluated using the periodic boundary conditions, where there is no obstruction at the exit, and the largest mass flow rate is achieved. To determine the largest possible pressure ratio, the exit of the compressor is completely blocked using specular boundary conditions. This second set of simulations gives  $\frac{P_{outlet}}{P_{inlet}} = \frac{P_{HI}}{P_{LO}}$ . Although it is impossible for the maximum flow rate and maximum pressure ratio to occur simultaneously, these values were used to give an upper limit on the isothermal work that can be extracted,  $\dot{W}_{iso} = \dot{m}RT_{amb} \ln \frac{P_{HI}}{P_{LO}} = \dot{m}RT_{amb} \ln P_{ratio}$ . The heat input is determined by summing the negative values of heat flux over the boundary cells (the normal vector points outward, so heat input is negative) and multiplying by the length of the boundary. The work is then divided by the heat input to yield an efficiency denoted by  $\eta_{iso} = \frac{\dot{m}RT_{amb} \ln(P_{ratio})}{\dot{Q}_{in}}$ .

The theoretical model assumes that the gas moves through the system slowly enough that it fully heats up to the hot temperature by the time it reaches the middle of the compressor, and cools to the low temperature by the exit (Figure 5-4a). The simulation, however, shows that the gas is cooler than its hot boundaries toward the center of the compressor, and is hotter than them near the cool edges (see Figure 5-4b).

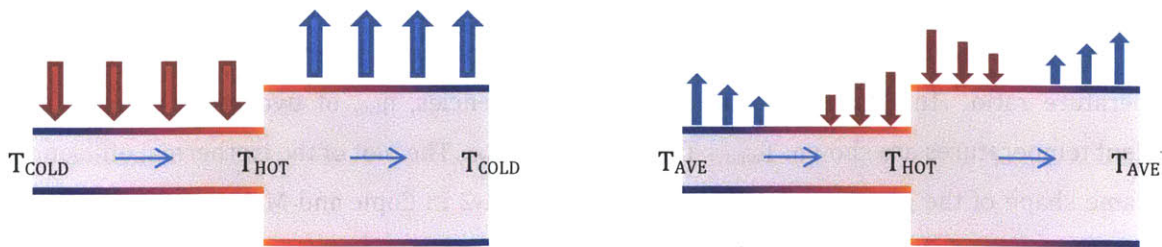


Figure 5-4: a. Theoretical Heat Input

b. Simulated Heat Input

Because the gas does not fully cool down, and is actually closer to  $T_{ave}$  at the exit of the pump, one cannot assume that a turbine located at the pump exit would operate isothermally at  $T_{cold}$ . However, the isothermal work was still used as an approximation; as we will see in Section 5.2.2, the efficiencies for the  $T_{amb} = T_{cold}$  and  $T_{amb} = T_{ave}$  cases did not differ significantly.

Alternatively, the energy “used” by the device may be approximated by  $T_{cold}S_{tot}$ , where  $S_{tot}$  is the net entropy generated by the device. This choice would correspond to a lower bound for heat transfer, and therefore an upper bound for the efficiency. We will refer to this efficiency as

$\eta_s = \frac{\dot{m}RT_{amb}\ln\left(\frac{P_{HI}}{P_{LO}}\right)}{T_{cold}S_{tot}}$ . If  $T_{hot}S_{tot}$  is substituted for  $T_{cold}S_{tot}$ , the resulting efficiency was found to correspond closely with  $\eta_{iso}$ .

The values for efficiency defined by the isentropic work are significantly lower than the ones shown in Figure 5-2, which are approximations of the flow work. To the extent that the approximate expression 5.1-2 represents the flow work correctly, this implies that the device works well as a pump, generating mass flow without a pressure rise. However, it is much less efficient when working as a compressor, which creates a significant pressure ratio. To measure the efficacy of the device as a pump, we might use  $\dot{W}_{fl} = \dot{m}RT_{amb}$ . This is the work required to displace a gas at a constant pressure, at can be derived as follows:

$$\begin{aligned}\dot{W}_{fl} &= P_{amb}(\dot{V}_{\rightarrow} - \dot{V}_{\leftarrow}) \\ \dot{W}_{fl} &= \rho RT_{amb}\dot{V}_{net} \\ \dot{W}_{fl} &= \dot{m}RT_{amb}\end{aligned}\tag{5.1-4}$$

As before, a measure of the efficiency is obtained by dividing by the heat input; the resulting efficiency is denoted  $\eta_{fl} = \frac{\dot{m}RT_{amb}}{\dot{Q}_{in}}$ . This efficiency is useful for measuring how effectively the pump can produce a flow.

## 5.2 RESULTS AND DISCUSSION

### 5.2.1 VARIATION WITH TEMPERATURE RATIO

As discussed in the theory section, the efficiency of the device increases with increasing temperature ratio. In Figure 5-5, the isothermal efficiencies,  $\eta_{iso}$ , of two cases with different ambient temperatures are shown:  $T_{amb} = T_{cold}$  and  $T_{amb} = T_{ave}$ . The plot of the isothermal efficiency is the same shape of the graph as shown using equation 5.1-2 in Copic and McNamara’s paper [26], shown in Figure 5-2. However, simulated efficiencies are much lower than the theoretical efficiencies calculated by Copic and McNamara [26]. This is likely due to differences in the



definition of efficiency, the difference in the assumed geometry, and the fact that the simulation is not in the ballistic regime.

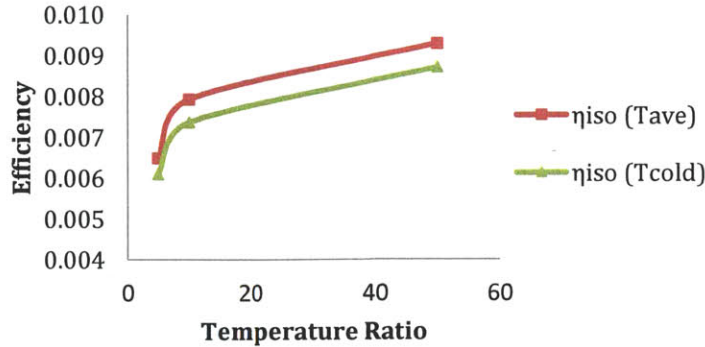


Figure 5-5: Variation of Isothermal Efficiency with Temperature Ratio

### 5.2.2 AMBIENT TEMPERATURE: COLD OR AVERAGE

In this section, we examine quantitatively the effect of the ambient temperature on the compressor. This was examined qualitatively in terms of its effect on mass flow rate and pressure ratio in Section 4.4.2. The percentage discrepancy in the work, mass flow rate, pressure ratio, and the three definitions of efficiency were quantified by  $\frac{|X_{T_{ave}} - X_{T_{cold}}|}{\max(X_{T_{ave}}, X_{T_{cold}})} \times 100\%$ , where  $X$  is the property being evaluated. The maximum percentage differences are shown in Table 5-1.

Table 5-1: Maximum Difference between Properties with  $T_{amb} = T_{ave}$  and  $T_{amb} = T_{cold}$

Property	% Difference
Mass flow [kg/m/s]	18.772
$P_{ratio}$	0.276
Work [W/m]	18.464
$Q_{in}$ [W/m]	18.469
$\eta_{iso}$	6.724
$\eta_s$	4.907
$\eta_{fl}$	1.963

From the table, it is apparent that the mass flow rate, the work, and the heat input can be significantly different between the cold and average ambient temperature cases. However, it is also apparent that the discrepancy in pressure ratio, and in the efficiencies, is relatively small. Because the value of work changes almost proportionally to the value of heat input, the ratio of the two, i.e.

the efficiency, remains relatively constant. We will therefore continue using only the efficiencies calculated from the cases where  $T_{amb} = T_{ave}$ .

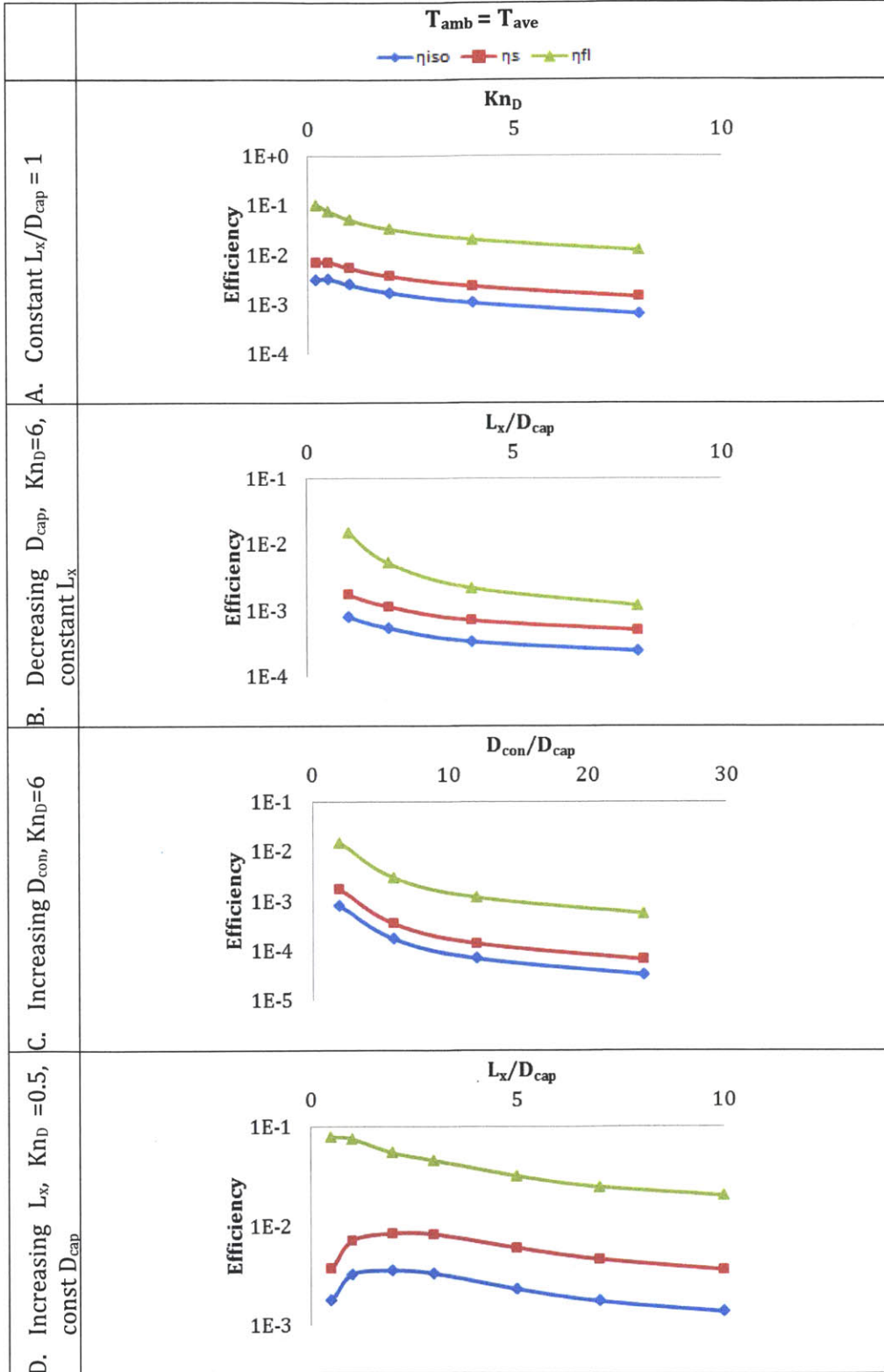
### 5.2.3 VARIATION OF EFFICIENCY WITH DIFFERENT PARAMETERS

Simulations were performed to determine how changing geometric parameters and the Knudsen number would affect the efficiency of the device. The different metrics for calculating efficiency in the cases where  $T_{amb} = T_{ave}$  are shown in Table 5-2. The efficiency based on displacement work, i.e. the pump's ability to produce a flow,  $\eta_{fl} = \frac{\dot{m}RT_{amb}}{\dot{Q}_{in}}$ , is the largest of the

efficiency definitions computed, and is on the same order of magnitude as Copic and McNamara's efficiency. It appears that the device is relatively efficient at pumping a gas, i.e. generating a mass flow, but generally less efficient at producing a pressure rise. The plots also show that

$\eta_{iso} = \frac{\dot{m}RT_{amb} \ln\left(\frac{P_{hi}}{P_{low}}\right)}{\dot{Q}_{in}}$  is lower than  $\eta_s = \frac{\dot{m}RT_{amb} \ln\left(\frac{P_{hi}}{P_{low}}\right)}{T_{cold}\dot{s}_{net}}$ . This is because in the first, only the heat input is considered, and the heat output is assumed to be wasted. The second, in contrast, uses the net entropy generated to approximate the net energy utilized. Additionally, recall that  $\eta_s$  is the upper bound for the entropy-based efficiency, as explained in Section 5.1. These simulations were performed at a fixed temperature ratio  $T_{ratio}=T_{hot}/T_{cold}=2$  ( $T_{hot}=398K$ ,  $T_{cold}=198K$ ,  $T_0=298K$ ).

**Table 5-2: Comparison of Different Definitions of Efficiency, for cases of  $T_{amb} = T_{ave}$**



From Table 5-2, we can see that the efficiency tends to decrease with increasing  $D_{con}/D_{cap}$ , which occurs in both rows B and C. There is a peak in  $\eta_{iso}$  and  $\eta_s$  with respect to  $Kn_D$  (row A), and when increasing  $L_x$  while holding  $D_{cap}$  constant (row D). In contrast,  $\eta_n$  decreases with increasing  $Kn_D$  and  $L_x/D_{cap}$ . It is clear that the maximum flow efficiency does not always occur at the same point as the maxima of the other efficiencies.

The peak values of  $\eta_{iso}$ ,  $\eta_s$ , and  $\eta_n$  are 0.35%, 0.83%, and 10.2%, respectively. The flow efficiency is much larger than the other efficiencies, as we expect. Table 5-3 compares the efficiency of various Knudsen compressors that exhibit optimal characteristics. Specifically, it compares Knudsen devices with maximum efficiency, work, mass flow rate and pressure ratio as well as minimum heat input. The highest  $\eta_{iso}$  and  $\eta_s$  are exhibited by a compressor of capillary Knudsen number ( $Kn_D$ ) 0.5, an  $L_x/D_{cap}$  of 2, and  $D_{con}/D_{cap}$  of 2. This device combines a respectable pressure rise with a large mass flow rate, and though it does not supply the maximum work of the cases simulated, it has a heat input small enough to raise its efficiency above the others. The case with the largest mass flow rate also exhibits the maximum work. As the isothermal work is directly proportional to the mass flow rate, but only proportional to the logarithm of the pressure ratio (see equation 5.1-3), it follows that a large mass flow rate is critical. When looking at flow work, the pressure ratio is not a factor (see equation 5.1-4), so the compressor with maximum mass flow rate has the maximum  $\eta_n$ . Note also that the case with the highest pressure ratio has the lowest efficiency.

**Table 5-3: Data for Knudsen devices with optimal characteristics,  $T_{amb} = T_{ave}$**

<b>Optimal:</b>	Mass flow Work, $\eta_n$	$P_{ratio}$	$Q_{in}$ $S_{tot}$	$\eta_{iso}$ $\eta_s$
$L_x/D_{cap}$ :	1	8	1	2
$D_{con}/D_{cap}$ :	2	16	2	2
$Kn_D$ :	0.2	6.0	8	0.5
<b>Mass flow [kg/m/s]:</b>	4.61E-06	3.34E-08	1.97E-08	1.21E-06
<b><math>P_{ratio}</math>:</b>	1.03	1.23	1.05	1.07
<b><math>Q_{in}</math> [W/m]:</b>	3.88	2.41	0.14	1.91
<b><math>S_{tot}</math> [W/m/K]:</b>	8.91E-03	5.90E-03	3.26E-04	4.09E-03
<b>Isothermal Work [W/m]:</b>	1.21E-02	5.84E-04	8.99E-05	6.74E-03
<b><math>\eta_{iso}</math> [%]:</b>	0.31	0.02	0.06	0.35
<b><math>\eta_s</math> [%]:</b>	0.68	0.05	0.14	0.83
<b><math>\eta_n</math> [%]:</b>	10.15	0.12	1.20	5.43

Although the maximum  $\eta_{iso}$  of 0.35% is small compared to photoelectric devices, note that the data in Table 5-3 correspond to the simple geometry shown in Figure 4-4, which is

straightforward to manufacture and requires no specialized materials. Additionally, this efficiency is based on  $T_{\text{ratio}}=2$ ; as we discussed above, the efficiency can be increased considerably if higher temperature ratios are used. Furthermore, if the device is being used primarily to move a fluid, then the efficiency is much higher:  $\eta_{\text{fl}} = 5.43\%$  when  $\eta_{\text{iso}} = 0.35\%$ .

The numbers for  $T_{\text{amb}} = T_{\text{cold}}$  are similar, and can be found in Section 8.2, in Appendix A.

## 6 SOLAR ENERGY: SPACE UTILIZATION

In this chapter, we briefly investigate some aspects arising from the possibility of using solar energy to power a Knudsen compressor. Specifically, we calculate the fraction of irradiated area that will be occupied by the compressors. In other words, we find the factor by which the solar energy would have to be concentrated to power a given Knudsen compressor.

### 6.1 THEORY

Assuming that the incoming solar radiation to 1 square meter of the earth is approximately 1000 W [27], we can determine the number of devices this energy can power, because we know how much energy each device requires to operate ( $Q_{in}$ ). A schematic of this 1 by 1 meter area is shown in Figure 6-1, with an array of  $N$  Knudsen compressors, each of length  $L_x$  and depth ( $W$ ) of 1 m. Multiplying the number of devices ( $N$ ) by the length ( $L_x$ ) of each device, and dividing by the total length (1 m), gives the amount of space that is used by the powered units. Equivalently, we could invert this quantity and generate the factor by which solar energy must be concentrated so that the incoming solar energy powers the region of space occupied by the devices.

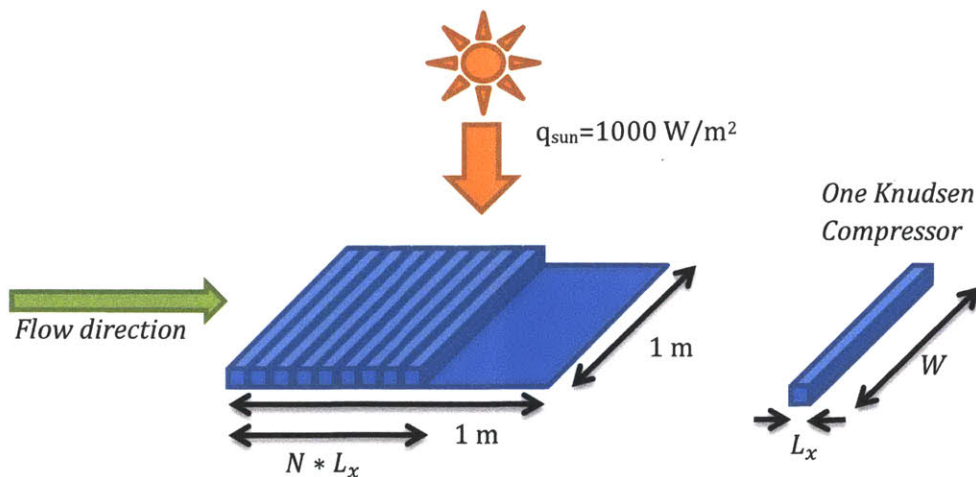


**Figure 6-1: Schematic for Calculation of Solar Flux Efficiency**

Note that our simulations assumed 2-dimensional devices; by setting the depth to one meter, we are essentially performing the calculation per unit depth. The depth of 1 meter is very large compared to the length of the device, which is on the order of a micrometer; this is consistent with our simulations, which were performed on 2-D (infinite depth) geometries.

## 6.2 RESULTS AND DISCUSSION

The fraction of space occupied by the compressors, based on an incoming solar flux of  $1000 \text{ W/m}^2$ , is shown in Table 6-1. The space used increases with increasing Knudsen number and increasing device length. Decreasing the  $D_{\text{con}}/D_{\text{cap}}$  increases the space utilization. The largest fraction of occupied space for  $T_{\text{amb}} = T_{\text{ave}}$  is  $1.27 \text{ E } -3$ , i.e. concentrating solar radiation by a factor of 790; for  $T_{\text{amb}} = T_{\text{cold}}$ , the maximum space utilization is  $1.54 \text{ E } -3$ , or a concentration of 649. In both cases, this occurs at  $L_x/D_{\text{cap}} = 1$ ,  $\text{Kn}_D = 8$  and  $D_{\text{con}}/D_{\text{cap}} = 2$ .



**Table 6-1: Variation of Fraction of Space Occupied with Different Parameters**

	$T_{amb} = T_{average}$ Fraction of Space Occupied	$T_{amb} = T_{cold}$ Fraction of Space Occupied
A. Constant $L_x/D_{cap}=1$		
B. Constant $L_x/D_{cap}=4$		
C. Decreasing $D_{cap}$ , $Kn_D=6$ , constant $L_x$		
D. Increasing $D_{con}$ , $Kn_D=6$		
E. Increasing $L_x$ , $Kn_D$ $=0.5$ , const $D_{cap}$		



## 7 CONCLUSION

A microscale Knudsen pump, or compressor, can be utilized to provide mass flow, and its opening can be constricted to provide a pressure rise. It was found that square channels in the capillary section are an optimal geometry to produce flow. According to our two-dimensional Low Variance Deviation Monte Carlo simulations, small capillary Knudsen numbers and short lengths tend to increase the mass flow rate but decrease the pressure rise. Increasing the diameter of the connector section with respect to the capillary section increases the pressure rise achieved by a single stage of the Knudsen compressor. According to the mathematical model in Muntz [22], the pressure ratio initially increases with Knudsen number, peaks, and then decreases again.

Large pressure rises can be achieved by constructing a multistage device that compounds a large number of Knudsen compressors. Changing the radius at each stage of the device to maintain a constant Knudsen number yields a higher pressure rise than keeping the radius constant.

In general, these devices are more efficient as pumps than as compressors. Although as a pump, efficiencies calculated for a small temperature ratio of 2 can be as high as 10%, as a compressor, the efficiencies are less than 1%. The isothermal compressor efficiency improves with increasing temperature ratio and decreasing ratio of connector to capillary diameter. It has an optimum with respect to Knudsen number and length to diameter ratio. The maximum isothermal efficiency of 0.35% occurs at  $Kn_D = 0.5$ ,  $D_{con}/D_{cap} = 2$  and  $L_x/D_{cap} = 2$  for the device simulated at a temperature ratio of 2.

As the ratio of connector to capillary diameter increases, the space utilization of the device decreases. Larger capillary Knudsen numbers allow for more space utilization. The larger the fraction of space occupied, the less the solar radiation must be concentrated to power the devices.

## 8 APPENDIX A: SELECTED DATA

### 8.1 ADDITIONAL STATISTICAL DATA:

In this section, we list additional simulation data obtained via LVDSMC simulations for the case where  $T_{\text{ratio}} = 2$ ,  $T_{\text{hot}} = 398$  K,  $T_{\text{cold}} = 198$  K,  $T_{\text{amb}} = 298$  K. This further validates the statement in Section 4.4.3 that  $Q_{\text{flux}}$  and  $Q_{\text{total}}$  are the only parameters which have large standard deviations relative to their mean value, implying that the net heat flux and transfer are close to zero.

#### Periodic Boundary Conditions: Maximum Flow Rate

	$L_x/D_{\text{cap}} = 10$ $Kn_{Ly} = 0.5$		$L_x/D_{\text{cap}} = 10$ $Kn_{Ly} = 10$		$L_x/D_{\text{cap}} = 1$ $Kn_{Ly} = 0.5$		$L_x/D_{\text{cap}} = 5$ $Kn_{Ly} = 0.5$		$L_x/D_{\text{cap}} = 50$ $Kn_{Ly} = 0.2$	
	mean value	std dev	mean value	std dev	mean value	std dev	mean value	std dev	mean value	std dev
$L_x/D_{\text{cap}}$	10.0		10.0		1.0		5.0		50.0	
$Kn_{Ly}$	0.5		10.0		0.5		0.5		0.2	
$Kn_D$	0.5		10.0		0.5		0.5		1.0	
$D_{\text{con}}/D_{\text{cap}}$	2.0		2.0		2.0		2.0		10.0	
$L_x/L_y$	10.0		10.0		1.0		5.0		10.0	
$L_x$	1.77E-06		8.84E-08		1.77E-07		8.84E-07		4.42E-06	
$L_{x0}$	8.84E-07		4.42E-08		8.84E-08		4.42E-07		2.21E-06	
$L_y$	1.77E-07		8.84E-09		1.77E-07		1.77E-07		4.42E-07	
$L_{y0}$	8.84E-08		4.42E-09		8.84E-08		8.84E-08		3.98E-07	
$D_{\text{cap}}$	1.77E-07		8.84E-09		1.77E-07		1.77E-07		8.84E-08	
$N_x$	40	0	40	0	40	0	100	0	40	0
$N_y$	60	34.64	40	0	40	0	40	0	100	0
$u_{\text{cap}}$ [m/s]	2E+0	6E-2	1E+0	8E-3	9E+0	6E-3	4E+0	6E-3	1E+0	4E-2
massflow [kg/m/s]	4E-7	1E-8	9E-9	7E-11	2E-6	1E-9	7E-7	1E-9	1E-7	3E-9
$P_{\text{enter}}$ [Pa]	9E+4	0E+0	9E+4	0E+0	9E+4	0E+0	9E+4	0E+0	9E+4	0E+0
$P_{\text{exit}}$ [Pa]	9E+4	0E+0	9E+4	0E+0	9E+4	0E+0	9E+4	0E+0	9E+4	0E+0
$P_{\text{ratio}}$	1.000	0	1.000	0	1.000	0	1.000	0	1.000	0
$Q_{\text{flux}}$ [W/m <sup>2</sup> ]	8E+2	6E+2	-3E+2	2E+2	-1E+3	2E+3	8E+2	7E+2	-6E+3	2E+3
$S_{\text{flux}}$ [W/m <sup>2</sup> /K]	4E+3	2E+1	7E+3	8E-1	1E+4	6E+0	6E+3	3E+0	2E+3	6E+0
$Q_{\text{max}}$ [W/m <sup>2</sup> ]	3E+6	1E+4	5E+6	5E+3	8E+6	2E+3	5E+6	4E+3	2E+6	9E+3
$S_{\text{max}}$ [W/m <sup>2</sup> /K]	1E+4	6E+1	3E+4	3E+1	4E+4	1E+1	2E+4	2E+1	9E+3	5E+1
$Q_{\text{total}}$ [W/m]	-2E-3	1E-3	-1E-6	9E-6	-4E-4	3E-4	-7E-4	2E-4	-3E-2	5E-3
$S_{\text{total}}$ [W/m/K]	3E-3	1E-5	3E-4	1E-8	4E-3	1E-6	4E-3	6E-7	4E-3	2E-5
$Q_{\text{in}}$ [W/m]	2E+0	2E-3	1E-1	5E-6	2E+0	1E-4	2E+0	1E-4	2E+0	3E-3
$S_{\text{in}}$ [W/m/K]	4E-3	6E-6	3E-4	7E-9	5E-3	4E-7	5E-3	4E-7	5E-3	8E-6

$T_{ratio} = 2$ ,  $T_{hot} = 398$  K,  $T_{cold} = 198$  K,  $T_{amb} = 298$  K.

**Specular Boundary Conditions: Maximum Pressure Ratio**

	$L_x/D_{cap} = 10$ $Kn_{Ly} = 0.5$		$L_x/D_{cap} = 10$ $Kn_{Ly} = 10$		$L_x/D_{cap} = 1$ $Kn_{Ly} = 0.5$		$L_x/D_{cap} = 5$ $Kn_{Ly} = 0.5$		$L_x/D_{cap} = 50$ $Kn_{Ly} = 0.2$	
	value	std dev	value	std dev	value	std dev	value	std dev	value	std dev
$L_x/D_{cap}$	10.0		10.0		1.0		5.0		50.0	
$Kn_{Ly}$	0.5		10.0		0.5		0.5		0.2	
$Kn_D$	0.5		10.0		0.5		0.5		1.0	
$D_{con}/D_{cap}$	2.0		2.0		2.0		2.0		10.0	
$L_x/L_y$	10.0		10.0		1.0		5.0		10.0	
$L_x$	1.77E-06		8.84E-08		1.77E-07		8.84E-07		0.0	
$L_{x0}$	8.84E-07		4.42E-08		8.84E-08		4.42E-07		0.0	
$L_y$	1.77E-07		8.84E-09		1.77E-07		1.77E-07		0.0	
$L_{y0}$	8.84E-08		4.42E-09		8.84E-08		8.84E-08		0.0	
$D_{cap}$	1.77E-07		8.84E-09		1.77E-07		1.77E-07		0.0	
$N_x$	40	0.00	40	0.00	40	0.00	100	0.00	40	0.0
$N_y$	60	34.64	40	0.00	40	0.00	30	14.14	100	0.0
$u_{cap}$ [m/s]	-3E-1	1E-2	-1E-2	1E-2	8E-3	5E-3	-4E-2	2E-2	-6E-1	4E-2
massflow [kg/m/s]	-5E-8	2E-9	-1E-10	1E-10	1E-9	9E-10	-7E-9	3E-9	-5E-8	4E-9
Penter [Pa]	8E+4	4E+0	8E+4	8E+0	8E+4	4E+0	8E+4	3E+1	7E+4	6E+2
Pexit [Pa]	9E+4	5E+0	8E+4	1E+1	9E+4	1E+0	9E+4	1E+0	9E+4	4E+1
Pratio	1.072	0.000	1.082	0.000	1.044	0.000	1.075	0.000	1.243	0.0
$Q_{flux}$ [W/m <sup>2</sup> ]	5E+4	2E+3	1E+5	3E+2	5E+2	8E+2	1E+5	4E+2	2E+4	4E+3
$S_{flux}$ [W/m <sup>2</sup> /K]	4E+3	2E+1	7E+3	2E+0	1E+4	3E+0	7E+3	5E+1	2E+3	2E+1
$Q_{max}$ [W/m <sup>2</sup> ]	3E+6	8E+3	5E+6	1E+4	8E+6	4E+3	5E+6	2E+4	2E+6	9E+3
$S_{max}$ [W/m <sup>2</sup> /K]	1E+4	4E+1	3E+4	5E+1	4E+4	2E+1	2E+4	1E+2	9E+3	4E+1
$Q_{total}$ [W/m]	-3E-4	6E-4	9E-6	9E-6	2E-4	1E-4	9E-4	7E-5	-4E-3	6E-3
$S_{total}$ [W/m/K]	3E-3	5E-6	2E-4	2E-8	4E-3	5E-7	4E-3	1E-5	4E-3	2E-5
$Q_{in}$ [W/m]	2E+0	2E-3	1E-1	1E-5	2E+0	2E-4	2E+0	6E-3	2E+0	3E-3
$S_{in}$ [W/m/K]	4E-3	6E-6	3E-4	3E-8	5E-3	3E-7	5E-3	2E-5	5E-3	9E-6

## 8.2 OPTIMAL DATA FOR $T_{AMB} = T_{COLD}$

Data exhibiting optimal characteristics (e.g. maximum mass flow, minimum heat input) for  $T_{amb} = T_{ave}$  were given in Table 5-3. Below is the same table, for  $T_{amb} = T_{cold}$ .

**Table 8-1: Optimal Characteristics for cases where  $T_{amb} = T_{cold}$**

<b>Optimal:</b>	<b>Mass flow Work, <math>\eta_n</math></b>	<b><math>P_{ratio}</math></b>	<b><math>Q_{in}</math> <math>S_{tot}</math></b>	<b><math>\eta_{iso}</math> <math>\eta_s</math></b>
$L_x/D_{cap}$ :	1	8	1.0	3
$D_{con}/D_{cap}$ :	2	16	2.0	2
$Kn_D$ :	0.2	6.0	8.0	0.5
<b>Mass flow [kg/m/s]:</b>	<b>5.64E-06</b>	4.07E-08	<b>2.39E-08</b>	1.29E-06
$P_{ratio}$ :	1.03	1.23	1.06	1.08
$Q_{in}$ [W/m]:	3.20	1.97	0.11	1.64
$S_{tot}$ [W/m/K]:	7.04E-03	4.77E-03	2.60E-04	3.21E-03
<b>Isothermal Work [W/m]:</b>	<b>1.00E-02</b>	4.80E-04	<b>7.36E-05</b>	5.38E-03
$\eta_{iso}$ :	3.13E-03	2.43E-04	6.41E-04	3.29E-03
$\eta_s$ :	7.18E-03	5.08E-04	1.43E-03	8.47E-03
$\eta_n$ :	1.00E-01	1.17E-03	1.19E-02	4.49E-02

## 9 BIBLIOGRAPHY

- [1] Y.-L. Han, E. P. Muntz, A. Alexeenko and M. Young, "Experimental and Computational Studies of Temperature Gradient-Driven Molecular Transport in Gas Flows Through Nano/Microscale Channels," *Nanoscale and Microscale Thermophysical Engineering*, vol. 11, pp. 151-175, 2007.
- [2] Y. Sone, *Kinetic Theory and Fluid Dynamics*, Boston: Birkhauser, 2002.
- [3] O. Reynolds, "On certain dimensional properties of matter in the gaseous state," *Philosophical Transactions of the Royal Society B*, vol. 170, p. 727, 1879.
- [4] J. C. Maxwell, "On stresses of rarefied gases arising from inequalities of temperature," *Philosophical Transactions of the Royal Society A*, vol. 170, p. 231, 1879.
- [5] M. Knudsen, "Eine revision der gleichgewichtsbedingung der gase. Thermische molekularstromung," *Annales de Physique*, vol. 31, p. 205, 1910.
- [6] S. E. Vargo, E. P. Muntz and W. C. Tang, "The MEMS Knudsen Compressor as a Vacuum Pump for Space Exploration Applications," 11 April 1999. [Online]. Available: <http://trs-new.jpl.nasa.gov/dspace/bitstream/2014/17226/1/99-0655.pdf>. [Accessed 22 March 2012].
- [7] E. P. Muntz, M. Yong and S. E. Vargo, "Microscale Vacuum Pumps," in *The Handbook of MEMS*, 2nd ed., M. Gad-el-hak, Ed., CRC Press, 2006.
- [8] S. Takata, H. Sugimoto and S. Kosuge, "Gas Separation by Means of the Knudsen Compressor," *European Journal of Mechanics B/Fluids*, vol. 26, pp. 155-181, 2007.
- [9] S. E. Vargo, E. P. Muntz, G. R. Shiflett and W. C. Tang, "Knudsen Compressor as a Micro- and Macroscale Vacuum Pump without Moving Parts or Fluids," *J. Vac. Sci. Technol.*, vol. A, no. 17(4), pp. 2308-2313, 1999.
- [10] N. K. Gupta and Y. B. Gianchandani, "Thermal Transpiration in Zeolites: a Mechanism for Motionless Gas Pumps," *Appl. Phys. Lett.*, vol. 93, 2008.
- [11] S. McNamara and Y. B. Gianchandani, "On-Chip Vacuum Generated by a Micromachined Knudsen Pump," *JMEMS*, vol. 14, 2005.
- [12] P. Zhang and R. Du, "Design and Analysis of a New Energy Harvesting Device Based on Knudsen Effect," *Nanotechnology 2009: Biofuels, Renewable Energy, Coatings, Fluidics and Compact Modeling*, vol. 3, pp. 165-168, 2009.
- [13] C. Cercignani, *The Boltzmann Equation and its Applications*, New York: Springer-Verlag, 1988.

- [14] G. A. Bird, *Molecular Gas Dynamics and the Direct Simulation of Gas Flows*, Oxford: Clarendon Press, 1994.
- [15] G. A. Radtke, *Efficient Simulation of Molecular Gas Transport for Micro and Nanoscale Applications*, PhD Thesis, Mechanical Engineering, MIT, 2011.
- [16] G. A. Bird, "Approach to translational equilibrium in a rigid sphere gas," *Phys. Fluids*, vol. 6, p. 1518, 1963.
- [17] T. M. M. Homolle and N. G. Hadjiconstantinou, "A Low-variance Deviational Simulation Monte Carlo for the Boltzmann Equation," *Journal of Computational Physics*, vol. 226, pp. 2341-2358, 2007.
- [18] L. L. Baker and N. G. Hadjiconstantinou, "Variance Reduction for Monte Carlo Solutions of the Boltzmann Equation," *Physics of Fluids*, vol. 17, no. 051703, 2005.
- [19] G. A. Radtke and N. G. Hadjiconstantinou, "Variance-reduced Particle Simulation of the Boltzmann Transport Equation in the Relaxation-time Approximation," *Physical Review E*, vol. 79, no. 056711, 2009.
- [20] N. G. Hadjiconstantinou, G. A. Radtke and L. L. Baker, "On Variance-reduced Simulations of the Boltzmann Transport Equation for Small-scale Heat Transfer Applications," *Journal of Heat Transfer*, vol. 132, no. 112401, 2010.
- [21] G. A. Radtke, N. G. Hadjiconstantinou and W. Wagner, "Low-Noise Monte Carlo Simulation of the Variable Hard-Sphere Gas," *Physics of Fluids*, vol. 23, no. 030606, 2011.
- [22] E. P. Muntz, Y. Sone, K. Aoki, S. Vargo and M. Young, "Performance Analysis and Optimization Considerations for a Knudsen Compressor in Transitional Flow," *J. Vac. Sci. Technol.*, vol. A20, no. 1, pp. 214-224, 2002.
- [23] T. Doi, "Numerical Analysis of Poiseuille Flow and the Thermal Transpiration of a Rarefied Gas Through a Pipe with a Rectangular Cross Section based on the Linearized Boltzmann Equation for a Hard Sphere Molecular Gas," *J. Vac. Sci. Technol. A*, vol. 28, no. 4, pp. 603-612, 2010.
- [24] N. G. Hadjiconstantinou, "The Limits of Navier-Stokes Theory and Kinetic Extensions for Describing Small Scale Gaseous Hydrodynamics," *Physics of Fluids*, vol. 18, no. 111301, 2006.
- [25] Y.-L. Han and E. Muntz, "Experimental Investigation of micro-mesoscale Knudsen compressor performance at low pressures," *Journal of Vacuum Science and Technology B*, vol. 25, no. 3, pp. 703-714, 2007.
- [26] D. Copic and S. McNamara, "Efficiency Derivation for the Knudsen Pump with and without Thermal Losses," *J. Vac. Sci. Technol.*, vol. A, no. 27(3), pp. 496-502, 2009.

[27] J. W. Tester, E. M. Drake, M. J. Driscoll, M. W. Golay and W. A. Peters, "Solar Energy," in *Sustainable Energy: Choosing Among the Options*, Cambridge, Massachusetts, The MIT Press, 2005, p. 545.